

Magnetoelastic Properties of Cobalt-Nickel Thin Films

by

Abraham Anapolsky

B.S. (San Francisco State University) 1996

M.S. (University of California, Berkeley) 2000

A thesis submitted in partial satisfaction of the
requirements for the degree of

Doctor of Philosophy
in

Engineering-Materials Science and Mineral Engineering

in the

GRADUATE DIVISION

of the

UNIVERSITY OF CALIFORNIA, BERKELEY

committee in charge:

Professor Oscar D. Dubon, Chair

Professor Paul C. W. Chu

Professor Ronald Gronsky

Professor Adrian Lee

Spring 2004

The thesis of Abraham S. Anapolsky is approved:

Chair

Date

Date

Date

Date

University of California, Berkeley

Spring 2004

Abstract

Magnetoelastic Properties of Cobalt-Nickel Thin Films

by

Abraham Anapolsky

Doctor of Philosophy in Engineering-Materials Science and Mineral Engineering

University of California, Berkeley

Professor Oscar D. Dubon, Chair

Cobalt-nickel alloys show large values of magnetostriction, magnetocrystalline anisotropy, and a martensitic phase transformation at temperatures around 0 K. Collectively, these properties make Co-Ni alloys good candidates for the so-called giant magnetostrictive effect. Magnetostrictive (and giant magnetostrictive) alloys can be used to replace complex machinery (such as actuators) in micro-electromechanical systems (MEMS). For this reason, researchers have been investigating the magnetostrictive properties of thin films.

I grew and characterized films in the composition range Co: 10 wt% Ni to Co: 35 wt% Ni. Films were grown by electron beam evaporation and a variety of techniques including SEM, TEM, x-ray diffraction, and SQUID magnetometry were used to characterize the films.

A thorough background in elastic and non-elastic mechanisms of deformation (in relation to magnetostriction) is discussed. These topics include a semi-classical treatment of magnetoelasticity, superelasticity, and martensitic transformations.

An important result of this thesis is the complete magnetic and physical characterization for the entire range of Co-Ni thin films that undergo martensitic transformation. Extensive analysis of morphology, mi-

crostructure, phase, and magnetic data, developed a consistent picture of Co-Ni polycrystalline thin films in the composition range mentioned above.

Another important result was the development of a novel technique for measuring the value of the magnetostriction coefficient in thin films . The in-plane component of magnetostriction (λ_s^{ip}) is determined by fitting a theoretical model (based on the Stoner-Wohlfarth theory for uniaxial systems) to magnetization vs temperature (M vs T) data for cobalt-nickel thin films. My theoretical model predicts the effect of an imposed stress (or strain) on the in-plane component of saturation magnetization (M_s^{ip}). The imposed stress (or strain) is due to a mismatch in the coefficient of thermal expansion between the film and substrate. The fit is accomplished by using λ_s^{ip} as a fitting parameter. M vs T experiments were carried out on a variety of polycrystalline Co-Ni thin films grown on silicon oxide and silicon nitride.

Acknowledgements

I would like to extend my utmost gratitude towards Professors Paul Chu, Oscar Dubon, and Eugene Haller. They are responsible for guiding, advising, and supporting my doctoral work at Berkeley. Their generosity of time and resources made my journey into the professional world possible. Likewise, I gratefully acknowledge the members of the Haller group, in particular Jeff Beeman, who helped me along the way. Finally, a great-big thank you to all my friends and family who supported and encouraged me during the toughest times, and celebrated with me on the most joyous of occasions.

This work was supported by the Director, Office of Science, Office of Basic Energy Sciences, Division of Materials Sciences and Engineering, of the U. S. Department of Energy under Contract No. DE-AC03-76SF00098.

This document was typeset with L^AT_EX.

Contents

| | | |
|----------|--|-----------|
| 1 | Introduction | 1 |
| 1.1 | magnetostriction and applications of magnetostrictive materials . . . | 2 |
| 1.2 | possible mechanisms of giant magnetostriction | 2 |
| 1.2.1 | reversible martensitic transformations | 3 |
| 1.2.2 | reversible twin boundary motion (RTBM) | 4 |
| 1.3 | Co-Ni alloys as a model system for GM | 5 |
| 2 | Background | 7 |
| 2.1 | ordinary magnetostriction | 8 |
| 2.1.1 | Joule (isotropic) magnetostriction | 8 |
| 2.1.2 | magnetoelasticity theory | 11 |
| 2.2 | non-elastic contributions to magnetostriction | 17 |
| 2.2.1 | magnetic/magnetoelastic induced martensitic transformation . | 18 |
| 2.2.2 | deformation through twin boundary motion | 29 |
| 2.2.3 | reversible twin boundary motion | 32 |
| 2.3 | summary | 36 |
| 3 | Special Considerations in the Co-Ni Alloy System | 38 |
| 3.1 | crystallography of Co-Ni thin films | 39 |
| 3.2 | magnetoelastic contributions to magnetostriction for a Co-Ni thin film | 40 |
| 3.2.1 | $\langle 111 \rangle$ oriented cubic grains | 41 |

| | | |
|----------|--|-----------|
| 3.2.2 | <100> oriented cubic grains | 44 |
| 3.2.3 | hexagonal phase magnetostriction | 44 |
| 3.3 | non-elastic contributions to magnetostriction in Co-Ni | 46 |
| 3.4 | summary | 47 |
| 4 | Experimental Procedure and Material Analysis | 49 |
| 4.1 | thin-film preparation | 50 |
| 4.1.1 | substrate selection | 50 |
| 4.1.2 | heat treatment | 51 |
| 4.1.3 | film growth | 51 |
| 4.1.4 | microstructure and composition | 52 |
| 4.2 | structural analysis | 56 |
| 4.3 | magnetic measurements | 62 |
| 4.4 | magnetostrictive measurements | 63 |
| 4.4.1 | cantilever deflection | 64 |
| 5 | Results and Conclusions | 69 |
| 5.1 | cantilever deflection measurement of magnetostriction | 69 |
| 5.1.1 | experimental results | 70 |
| 5.2 | microstructure and film morphology | 72 |
| 5.3 | a novel magnetoelastic characterization technique | 75 |
| 5.3.1 | Application of the S-W model to Co-Ni thin films | 76 |
| 5.3.2 | Strain due to CTE mismatch | 77 |
| 5.3.3 | Results of uniaxial model | 80 |
| 5.4 | conclusions and future work | 85 |
| 5.4.1 | future work | 85 |
| 5.4.2 | conclusion | 87 |
| A | Linear deformation using the strain tensor representation | 89 |

| | |
|---|-----------|
| B Stress dependence of \vec{M}_{ip} | 91 |
| Bibliography | 93 |

List of Tables

| | | |
|-----|--|----|
| 1.1 | <i>Properties of selected magnetostrictive materials</i> | 3 |
| 2.1 | <i>Magnetoelastic values for cobalt, nickel, and iron.</i> | 18 |
| 3.1 | <i>Estimated maximum in-plane strain contributions for a textured Co-Ni thin film.</i> | 47 |
| 4.1 | <i>Summary of various Co-Ni films grown for this study</i> | 50 |
| 4.2 | <i>Diffraction pattern standards for nickel and cobalt</i> | 57 |
| 5.1 | <i>Magnetoelastic data for Co-Ni thin films.</i> | 84 |

Chapter 1

Introduction

In the 1970's research was done on using cobalt-nickel alloys for magnetic transducers [1, 2]. Co-Ni alloys were investigated because they exhibited large magnetocrystalline anisotropy which is a strong indicator of large magnetostriction. Magnetostrictive strains up to 10^{-4} were measured [1]. The intended application of these materials was as acoustic transducers for sonar and for ultrasonic transducers.

Recent developments in micro electromechanical systems (MEMS) [3, 4] combined with the discovery of so-called ferromagnetic shape memory alloys [5] highlight the need to investigate the phenomenon of giant magnetostriction in thin films. However, very few studies have been performed. The reason MEMS lend themselves to studying novel thin film magnetostrictive materials from a materials science standpoint is twofold:

1. Magnetostrictive transducers have several advantages over current MEMS transducers. Magnetostrictive transducers have no moving parts; they can be made of tough, metallic materials (as opposed to polysilicon); and they can be actuated remotely—that is, by an external field. This last point is important because it means that a MEMS actuator need not have an independent power source or be hard wired to an external power source.

2. Current MEMS research has focused on the mechanical and electrical engineering properties of the systems. While this is important in terms of device development, application of materials science principles can help to greatly expand the potential and application of MEMS technology. Magnetism and magnetic materials, in particular, lend themselves to the materials science approach.

1.1 magnetostriction and applications of magnetostrictive materials

Magnetostriction is a phenomenon in which a change in the state of magnetization of a sample is correlated with a change in shape. For isotropic materials the parameter characterizing the strain is λ_s , which is the measured linear strain in a material that has reached its saturation value of magnetization, M_s . Ordinary magnetostriction is characterized by strains $\sim 10^{-6}$ and elastic displacements [6]. Giant magnetostriction (GM) is characterized by large strains $\sim 10^{-3} - 10^{-2}$ and non-elastic¹ phenomenon.

Three main uses of magnetostrictive materials are 1) as transducers in both ultrasonic and sonar devices 2) in actuators for example, in hard drive read/write arms and 3) as acoustic wave resonators, for example, anti-theft tags. Table 1.1 gives a comparison of various magnetostrictive materials. A recent article by Szymczak [8] summarizes the current state of magnetostrictive materials and applications.

1.2 possible mechanisms of giant magnetostriction

Two important theories to account for GM, which have been investigated in bulk materials, are martensitic phase transformation (induced by an applied magnetic field) and reversible twin boundary motion.

¹An exception is the rare earth-iron alloys (such as Fe-Tb), $\lambda_s \sim 10^{-3}$ which have a proposed elastic mechanism [7]

| Material | λ_s (at M_s) | E (GPa) | Comments |
|---------------------|---------------------------------|---------|---|
| Fe-Te (+rare earth) | 10^{-3} (10 kOe) | 25-35 | Already in commercial use. Brittle and expensive |
| Fe-Ni | 10^{-5} (1 kOe) | 200 | Inexpensive |
| Ni-Mn-Ga | 10^{-2} (10 kOe) | na | Brittle, low operating temp. |
| Ni-Co | 10^{-3} (20 kOe) ^a | 200 | Tough, corrosion resistant. |

Table 1.1: *Selected magnetostrictive materials. λ_s is the value of maximum strain when the materials is fully magnetized (saturation).*

^asingle crystal, [001] oriented, at 175 K

1.2.1 reversible martensitic transformations

A martensitic transformation is a first order phase transformation, in the solid state, between two phases with similar crystal structures. This transformation is diffusionless and is said to be accomplished by a 'shear-like' mechanism. There are many excellent books and review articles written on martensitic transformations. Zenner [9] models how an application of a magnetic field to a ferromagnetic material can induce a martensitic transformation by a change in the free energy of the material. James and Hane [10] discuss the necessary conditions for this process in thin films.

For practical applications it is important to have a reversible martensitic transformation [11]. In this context, reversible means that the amount of material that is transformed from the parent phase (called austenite) to the daughter phase (martensite) is completely transformed back to austenite upon reversal of the driving force.

For example, a material begins (upon cooling) to transform to the martensite phase at a temperature M_S and finishes at a temperature $M_F < M_S$. This transformation would be perfectly reversible if upon heating the material above M_S the entire sample reverts back to the austenite phase.

Reversibility can also be accompanied by microstructural and gross shape (in one or both phases) recovery. This phenomenon is give the name 'shape memory effect' (SME).

1.2.2 reversible twin boundary motion (RTBM)

Twin boundary motion as a result of an applied stress is fairly well known to metallurgists. The specific case of a reversible deformation accompanied by twin boundary motion is known as pseudoelasticity² a term put forth by Christian [14]. The theory of twin boundary motion was developed by considering the effect of an external (applied) stress, and Christian proposed the following as the most probable explanation for reversibility in twin deformation: The twin that is converted into a more favorable variant does not completely vanish. Some part of it is retained (as a dislocation or small nucleus) and this defect provides a sufficient amount of elastic energy for the sample to reconfigure itself in the original twin configuration, which is the lowest energy configuration in the absence of external stress.

An awareness of pseudoelasticity is important in the case of large magnetoelastic effects because many authors have proposed replacing the external stress with a magnetoelastic stress (as the driving force). An alternate theory [15, 16] proposes that the driving force has to do with the alignment of favorable magnetic domains with the favorable twin domains.

In any case, the phenomenon has been reported on in numerous systems such as Ni-Mn-Ga [17, 18, 15] and Fe-Pt-Pd [19, 20]; and it is likely that some combination of the proposed effects are at work in systems displaying GM.

Only materials that undergo a martensitic transformation display pseudoelasticity and giant magnetostriction. In general, materials that undergo large reversible deformations are characterized as shape memory alloys (alloys displaying the SME). Ferromagnetic materials that undergo both the martensitic transformation and GM are called ferromagnetic shape memory alloys (FSMA). This topic will be discussed more thoroughly in chapter two.

²some authors refer to this as 'rubber like behavior (RLB) [12, 13]

1.3 Co-Ni alloys as a model system for GM

It can be shown that large magnetocrystalline anisotropy is one of the prime indicators of GM [21]. Therefore one would expect GM (by the phenomenon mentioned previously) to occur in materials that have large magnetocrystalline anisotropy and display the martensitic transformation. Further, for practical considerations it would be advantageous to have a material that is easy to prepare, has moderate transformation temperatures ($\sim 300\text{K}$)³, and good mechanical properties. Co-Ni alloys represent such a system. They have excellent mechanical properties, high anisotropy, and for compositions in the range of Co: 33 wt% Ni, martensitic transformation temperatures around room temperature.

Recent experiments done on bulk Co-Ni [22] have shown such alloys to have a reversible magnetostriction of ~ 0.01 at applied fields of ~ 1 T. However, the martensitic transformation temperature is reported to be 170 K. This value of M_s does not agree with values found in the literature and is much too low for practical uses of this material. GM has also been reported in Ni-Al-Co alloys [23], which have a more complex transformation path and microstructure than Co-Ni but have less desirable mechanical properties. Even though favorable values of GM in Co-Ni alloys have been reported, a strong argument for a particular mechanism has not been proposed. Thus, much work remains to be done on this material.

Observing the phenomenon of giant magnetostriction in a relatively simple alloy will help towards a fundamental understanding of the mechanisms of GM in thin films. This is the objective of current investigations, which will proceed along two paths. First, a range of Co-Ni alloys will be chosen, and thin films will be prepared by evaporation in a UHV chamber.

Various deposition methods will be employed such as co-deposition, multi-layer/annealing,

³To take advantage of a reversible martensitic transformation the material should have M_s around room temperature for, but for RTBM, M_s should be high enough that the material is in the twinned microstructure at RT.

and congruent evaporation from alloy sources. These techniques will be used to control composition and film microstructure.

Second, after suitable characterization of composition and structure, direct measurement of magnetostrictive properties will be performed. These experiments intend to document phase transformation, microstructural change, and strain-temperature-magnetization behaviors.

Chapter 2

Background

At this point it is important to bring up the main idea behind this thesis, namely, to measure and predict the shape change (expressed as a strain) in Co-Ni thin films resulting from the application of a magnetic field. I will adopt the term "magnetostriction" to cover all aspects of shape change induced by a magnetic field. Whether these concepts be conventional magnetostriction, or derivatives of the body stresses and changes in free energy that have been attributed to magnetostriction, will be stated explicitly.

In order to describe the complete phenomenon of magnetostriction in thin film Ni-Co alloys, the following topics must be described and integrated with physical data on the Ni-Co system:

- Ordinary magnetostriction (magnetoelasticity)
- Non-elastic mechanisms of magnetostriction

The first subject is fairly well understood by existing theories of magnetism and elasticity, and thus a review of magnetoelasticity will be geared towards the system (cubic, ferromagnetic) at hand. The second subject is less familiar and warrants a few introductory comments.

Non-elastic mechanisms of magnetostriction have to do with the coupling of magnetostrictive stresses and magnetic energy with behavior such as dislocation motion and phase transformation. In chapter three, the numerical values of magnetostriction (from various sources) for the Co-Ni system will be calculated.

2.1 ordinary magnetostriction

Conventional magnetostriction is defined as an *elastic* response to a change in magnetization. This is a very broad definition, and it covers magnetoelastic coupling in all materials. For purposes of this thesis, I will limit the foregoing discussion to ferromagnetic materials, although the basic arguments describing Joule magnetostriction apply to all materials.

2.1.1 Joule (isotropic) magnetostriction

Magnetostriction was first observed in isotropic¹ materials, and it was found that the amount of strain, $\frac{\partial l}{l}$, could be closely predicted by

$$\frac{\partial l}{l} = \frac{3}{2}\lambda_s(\cos^2 \theta - \frac{1}{3}) \quad (2.1)$$

where λ_s is the magnetostriction when the material has reached a saturation value of magnetization and is a materials constant, and θ is the angle between the direction the strain is measured in and the direction of magnetization \vec{M} , (figure 2.1). In the following sections this relation will be derived from first principles by considering the contributions of magnetization and strain to the free energy.

The problem with describing magnetostriction lies in finding a mechanism that relates strain to magnetization. I will try to describe the microscopic causes of mag-

¹polycrystalline materials that can be treated as approximately isotropic for certain magnetostrictive measurements

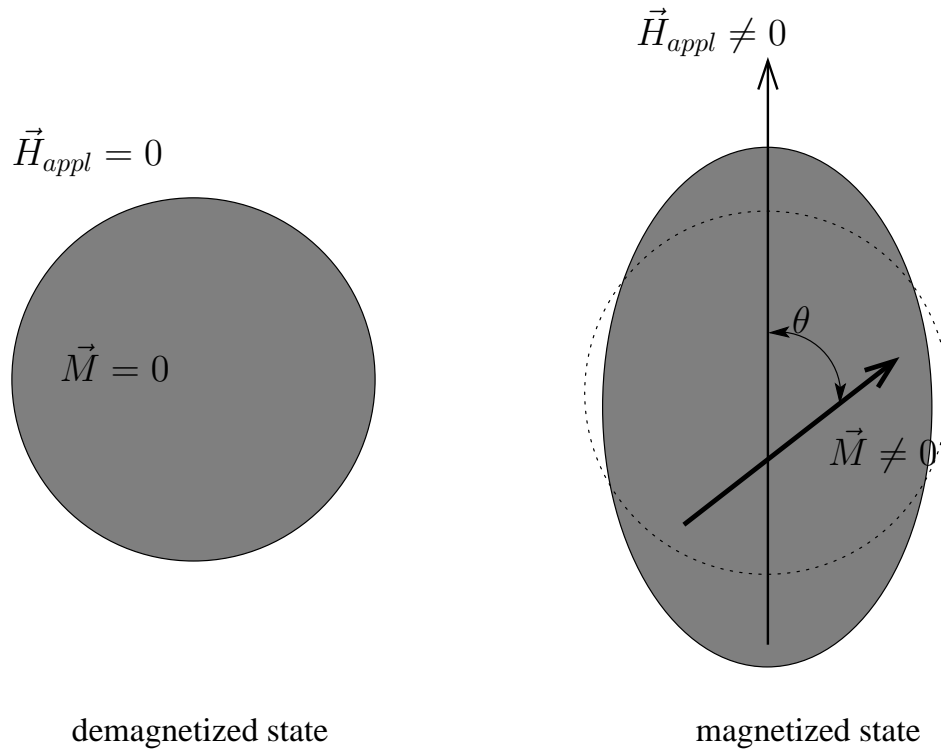


Figure 2.1: *Illustration of Joule magnetostriction. Strain is measured parallel to the applied field, \vec{H} , relative to the macroscopic magnetic moment (or magnetization), \vec{M}*

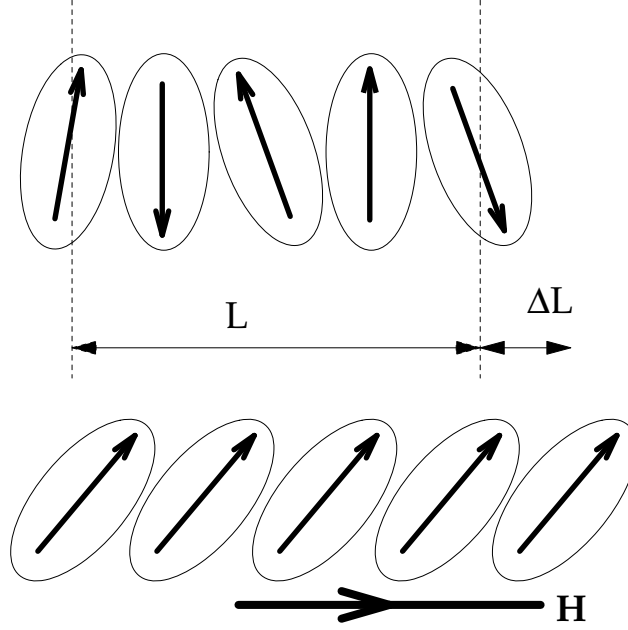


Figure 2.2: *Top view shows a collection of magnetic atoms in an unmagnetized state. At bottom, the atoms have a net magnetization. The magnetization can arise spontaneously (as in a material cooled below T_c) or be induced by an applied field*

netostriction conceptually and save the calculations for describing the macroscopic phenomenon. Cullity [6] provides an intuitive description that nicely illustrates the basic concepts. Figure 2.2 depicts an arrangement of atomic magnetic moments with no net magnetization (top) and in a magnetized state (bottom). The two important ideas here are that the atoms are not spherically symmetric and the direction of the magnetic moment is coupled with the orientation of the atom; this results in a change in length, ΔL , of the assembly of atoms.

Figure 2.3 shows the magnetostrictive behavior of a typical ferromagnetic material as a function of magnetization. In this example a domain process of magnetization is assumed. Thus, the portion marked as forced magnetostriction refers to a small increase in strain due to dipole rotation after favorable magnetic domains have ceased to grow. In general, more emphasis is placed on understanding the saturation value of magnetostriction than on understanding the functional dependence on magnetization.

The reason for this is primarily based on the fact that most materials used in magnetostriction applications achieve saturation at relatively low fields. In addition, the path to magnetic saturation is not unique and can be changed by materials processing or changes in sample shape and orientation. Thus, there may be several distinct relationships between \vec{M} and $\lambda(\vec{M})$ but the magnetostrictive *constants* are material and symmetry dependent.

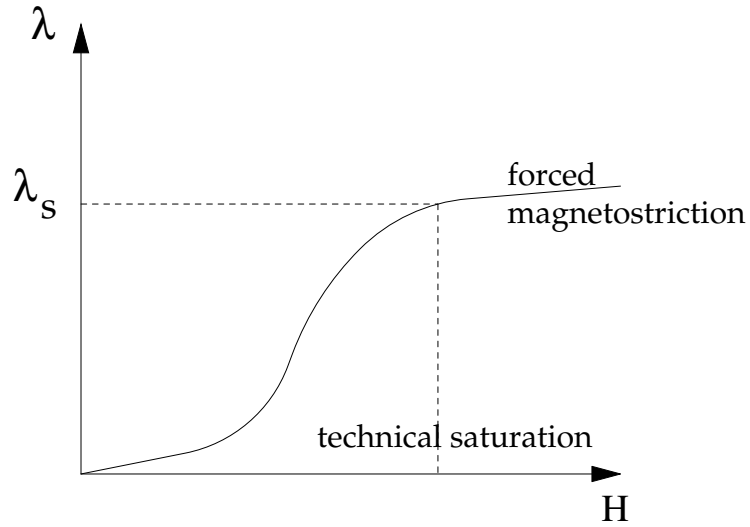


Figure 2.3: *Magnetostriction as a function of applied field for a typical ferromagnetic material.*

In general, the degree of magnetostrictive strain is correlated with the process of magnetization, and therefore the state of strain can vary widely. However, the important thing to note is the fact that at saturation, the magnetostrictive stress asymptotically approaches a theoretically predictable value.

2.1.2 magnetoelasticity theory

Now that the concept of magnetostriction has been introduced, we have to examine the underlying microscopic process and apply the resulting theory to ideal (for now) materials—in particular, the cubic and hexagonal systems.

Figure 2.4 schematically illustrates the atomistic process that leads to magnetostriction. As the direction of the magnetization is rotated, the moment associated with a magnetic orbital is also rotated which results in a change of the orbital direction via spin-orbital (L-S) coupling. The change in orbital direction shows up as a change in bond position (and direction). The shape change associated with the changing bond position can manifest as a strain or a volumetric change. The follow-

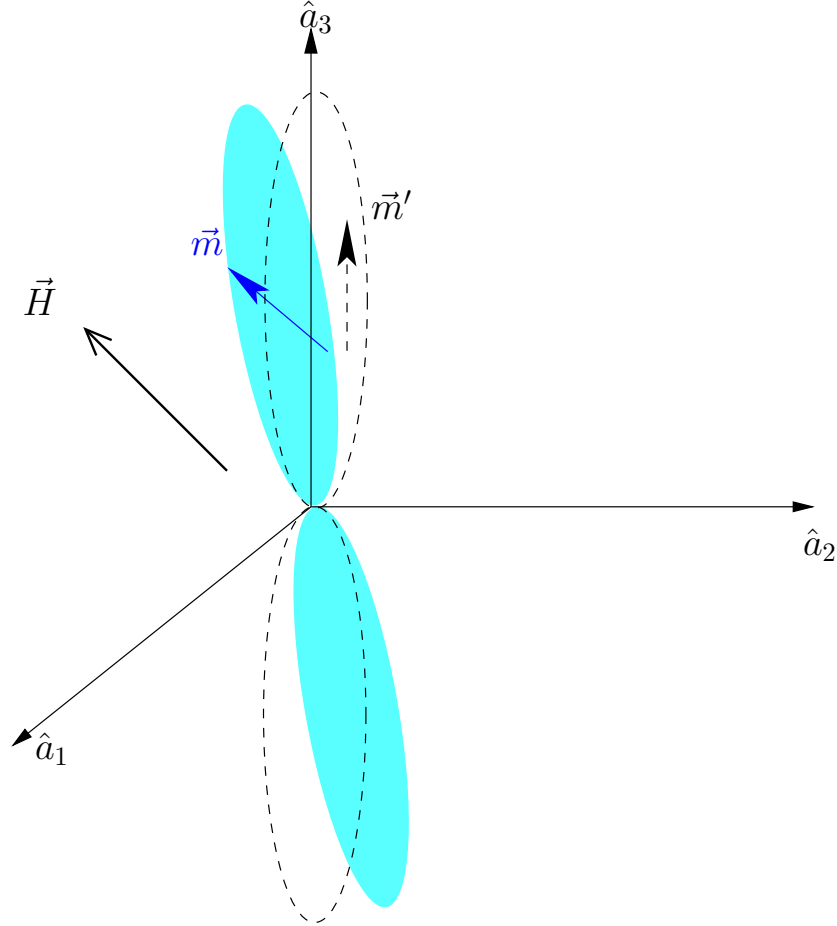


Figure 2.4: *Dashed outline shows equilibrium atomic position with respect to crystal axes. Upon application of an external magnetic field, sufficient to saturate the material, the net atomic magnetic moment, \vec{m} , is parallel to the applied field, \vec{H} . The atom has also changed position due to L-S coupling. Opposing this shift in position is the elasticity of the lattice, this interaction is the magnetoelastic effect.*

ing is a derivation based on the texts of Chen [24], Chikazumi [25], and O’Handley [21].

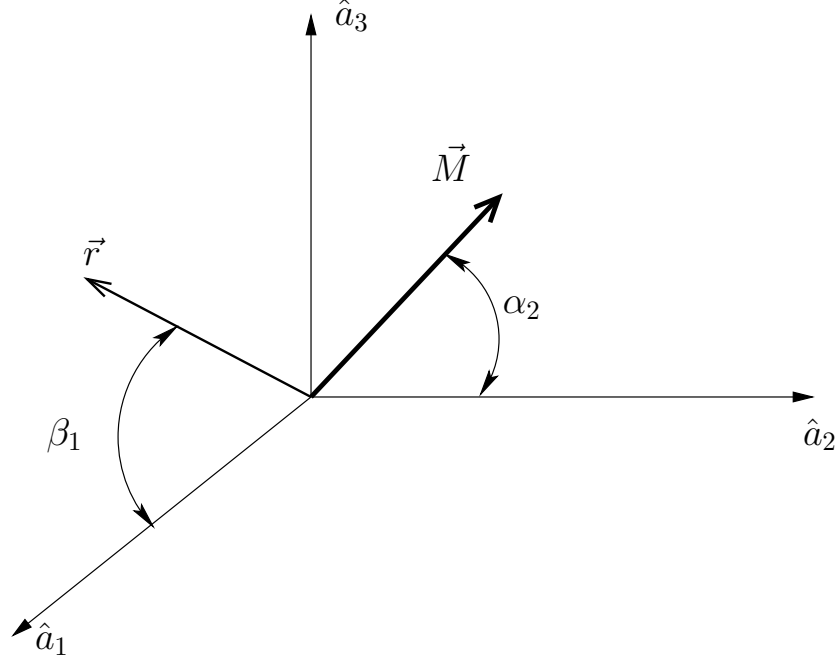


Figure 2.5: *Geometry for magnetoelastic calculations. α_i is defined by $\hat{a}_i \bullet \vec{M}$, that is, α_i is the cosine of the angle between \hat{a}_i and \vec{M} . For β , the same definition holds with \vec{r} substituted for \vec{M} . The vector \vec{r} represents the direction of strain measurement with respect to the crystal axes.*

The goal of the following calculations is to determine the components of the *magnetostrictive strain tensor*, b_{ij} . The components of b_{ij} involve the magnetoelastic constants, the elastic constants, and the angle that the magnetization makes with the crystal axes. When b_{ij} is projected onto a crystal direction \hat{r} , the direction of strain measurement and the value of magnetostriction can be predicted. Figure 2.5 shows the geometrical construction for these quantities.²

The components of b_{ij} are derived from minimizing the magnetoelastic free energy with respect to the various strains. The magnetoelastic free energy for a system with

²In practice, the values of magnetostriction is carefully measured in different directions for a single crystal and these values determine the coefficients of b_{ij} .

cubic symmetry ³ is [24]

$$\begin{aligned}
u_{me} = & B_1(e_{xx}(\alpha^2_1 - \frac{1}{3}) + e_{yy}(\alpha^2_2 - \frac{1}{3}) + e_{zz}(\alpha^2_3 - \frac{1}{3})) \\
& + B_2(e_{xy}\alpha_1\alpha_2 + e_{yz}\alpha_2\alpha_3 + e_{xz}\alpha_1\alpha_3) \\
& + \frac{1}{2}c_{11}(e_{xx}^2 + e_{yy}^2 + e_{zz}^2) + c_{12}(e_{xx}e_{yy} + e_{yy}e_{xx} + e_{xx}e_{zz}) \\
& + \frac{1}{2}c_{44}(e_{xy}^2 + e_{yz}^2 + e_{xz}^2)
\end{aligned} \tag{2.2}$$

B_i and c_{ij} are the magnetoelastic and elastic coefficients respectively; and α is defined in figure 2.5. In order to solve for the e_{ij} , take $\frac{\partial u_{me}}{\partial e_{ij}} = 0$. This leads to six equations (b_{ij} is Hermitian) of two types:

$$\begin{aligned}
& i = j \\
\frac{\partial u_{me}}{\partial e_{ii}} = & B_1(\alpha^2_i - \frac{1}{3}) + c_{12}(e_{jj} + e_{kk}) = 0 \\
& i \neq j \\
\frac{\partial u_{me}}{\partial e_{ij}} = & B_2\alpha_i\alpha_j + c_{44}e_{ij} = 0
\end{aligned} \tag{2.3}$$

In equation 2.3 the solutions for e_{ij} have the form

$$e_{ij} = -B_2 \frac{\alpha_i \alpha_j}{c_{44}}$$

and the solutions for the e_{ii} are

$$e_{ii} = -B_1 \frac{\alpha_i^2 - \frac{1}{3}}{c_{11} - c_{12}}$$

On inspection, this gives the result that the diagonal components of $\frac{\partial u_{me}}{\partial e_{ij}}$ are the cubic

³This expression for free energy is based on expanding u_{me} in terms of the direction cosine, α , and retaining terms to second order in α .

stresses plus a 'magnetic stress', $B_1(\alpha_i^2 - \frac{1}{3})$. Complementary to these strains are the non-diagonal components, which represent a 'magnetic shear', $B_2 e_{ij} \alpha_i \alpha_j + c_{44} e_{ij}$ plus the normal elastic cubic shear. This makes physical sense because the free energy takes the form of an elastic energy plus a magnetic term, which when differentiated gives the well known result for stress in cubic systems [26], combined with the magnetic analogue of Hooke's law.

Now we define the magnetostrictive stress tensor⁴ as $b_{ij} \equiv e_{ij}$ where

$$b_{ij} = \begin{pmatrix} -B_1 \frac{(\alpha_1^2 - \frac{1}{3})}{(c_{11} - c_{12})} & -B_2 \frac{\alpha_1 \alpha_2}{c_{44}} & -B_2 \frac{\alpha_1 \alpha_3}{c_{44}} \\ -B_2 \frac{\alpha_1 \alpha_2}{c_{44}} & -B_1 \frac{(\alpha_2^2 - \frac{1}{3})}{(c_{11} - c_{12})} & -B_2 \frac{\alpha_2 \alpha_3}{c_{44}} \\ -B_2 \frac{\alpha_1 \alpha_3}{c_{44}} & -B_2 \frac{\alpha_2 \alpha_3}{c_{44}} & -B_1 \frac{(\alpha_3^2 - \frac{1}{3})}{(c_{11} - c_{12})} \end{pmatrix}. \quad (2.4)$$

To find $\frac{\partial l}{l}$, project b_{ij} onto the unit vector β . This gives the following (for a proof see appendix A),

$$\begin{aligned} \frac{\partial l}{l} = & -\frac{B_1}{(c_{11} - c_{12})} (\alpha_1^2 \beta_1^2 + \alpha_2^2 \beta_2^2 + \alpha_3^2 \beta_3^2 - \frac{1}{3}) \\ & -\frac{B_1}{c_{44}} (\alpha_1 \alpha_2 \beta_1 \beta_2 + \alpha_2 \alpha_3 \beta_2 \beta_3 + \alpha_3 \alpha_1 \beta_3 \beta_1) \end{aligned} \quad (2.5)$$

This elegant result for cubic materials can best be illustrated by example. When the sample is magnetized in the [100], [111], and [110] directions and the strain is also measured in these directions, we get the following results:

For the [100] type directions

$$\begin{aligned} \alpha_1 = \beta_1 = 1; \alpha_{i \neq 1} = \beta_{i \neq 1} = 0 \\ \frac{\partial l}{l} \equiv \lambda_{100} = -\frac{2}{3} \frac{B_1}{c_{11} - c_{12}} \end{aligned} \quad (2.6)$$

⁴The minus sign is consistent with the convention that negative strains result from positive forces

For the $[111]$ type directions

$$\begin{aligned}\alpha_i &= \beta_i = \frac{1}{\sqrt{3}} \\ \frac{\partial \ell}{\ell} &\equiv \lambda_{111} = -\frac{1}{3} \frac{B_2}{c_{44}}\end{aligned}\tag{2.7}$$

And for the $[110]$ type directions

$$\begin{aligned}\alpha_1 &= \beta_1 = \alpha_2 = \beta_2 = \frac{1}{\sqrt{2}}; \alpha_3 = \beta_3 = 0 \\ \lambda_{110} &= -\frac{1}{6} \frac{B_1}{c_{11} - c_{12}} - \frac{1}{4} \frac{B_2}{c_{44}} = \frac{1}{4} \lambda_{100} + \frac{3}{4} \lambda_{111}\end{aligned}\tag{2.8}$$

As the last example suggests, the other λ_{ijk} can be expressed as combination of λ_{100} and λ_{111} . Often the elastic/magnetoelastoc coefficients in equation 2.5 are replaced with the magnetostriction constants, e.g.

$$\frac{B_1}{c_{11} - c_{12}} = -\frac{3}{2} \lambda_{100}$$

As would be expected, λ_{111} depends on the shear modulus, c_{44} .

For cubic materials that are isotropic, $\lambda_{100} = \lambda_{111} = \lambda_0$ and equation 2.5 is simplified by

$$\begin{aligned}((\alpha_1 \beta_1)^2 + (\alpha_2 \beta_2)^2 + (\alpha_3 \beta_3)^2) &= \cos^2 \theta \\ \alpha_i \beta_j &= 0.\end{aligned}$$

Here, θ is the angle between the direction of magnetization and the direction of strain measurement. Thus, the strain takes the form

$$\frac{\partial l}{l} = \lambda_0 (\cos^2 \theta - \frac{1}{3})$$

which is the same as equation 2.1. For polycrystalline materials averaging over the possible values gives a prediction of the saturation value of magnetostriction. For example polycrystalline cubic materials have

$$\lambda_s^{pc} = \frac{2}{5}\lambda_{100} + \frac{3}{5}\lambda_{111}. \quad (2.9)$$

The preceding derivation can be repeated for hexagonal materials with the only differences being in the symmetry of the terms. Chen [24] gives the value of magnetostriction for hexagonal materials as

$$\begin{aligned} \frac{\partial l}{l} = & \lambda_A[(\alpha_1\beta_1 + \alpha_2\beta_2)^2 - (\alpha_1\beta_1 + \alpha_2\beta_2)\alpha_3\beta_3] \\ & + \lambda_B[(1 - \alpha_3^2)(1 - \beta_3^2) - (\alpha_1\beta_1 + \alpha_2\beta_2)^2] \\ & + \lambda_C[(1 - \alpha_3^2)\beta_3^2 - (\alpha_1\beta_1 + \alpha_2\beta_2)\alpha_3\beta_3] \\ & + 4\lambda_D(\alpha_1\beta_1 + \alpha_2\beta_2)\alpha_3\beta_3 \end{aligned} \quad (2.10)$$

To conclude this discussion, table 2.1 gives values of magnetoelastic and magnetostrictive constants for iron, nickel, and cobalt.

2.2 non-elastic contributions to magnetostriction

While the previous section described a well known phenomenon, magnetoelasticity, with compiled physical data for many materials, this section will discuss concepts that are not well understood, unmeasured, and some instances, hypothetical.

| Quantity | Fe ^a | Ni | FCC Co | $\lambda_i^{hex}(\times 10^{-6})$ | HCP Co ^b |
|--|-----------------|------|--------|-----------------------------------|---------------------|
| $\mu_0 M_s^2/2(\times 10^6)$ (J/m ³) | 1.9 | 0.14 | 1.3 | | 1.3 |
| $B_1(\times 10^6)$ (N/m ²) | -2.9 | 6.2 | -16 | λ_A | 45 |
| $B_2(\times 10^6)$ (N/m ²) | 2.9 | 4.3 | 26 | λ_B | 95 |
| $\lambda_{100} \times 10^{-6c}$ | 21 | -46 | 75.6 | λ_C | 110 |
| $\lambda_{111} \times 10^{-6}$ | -21 | -24 | -118 | λ_D | 100 |

Table 2.1: *Selected magnetoelastic values. The quantity $\mu_0 M_s^2/2$ is the energy it takes to magnetize the material to saturation in the easy direction.*

^aValues for Fe, Ni, and FCC Co from O’Handley [21]

^b[24]

^call values for room temperature

2.2.1 magnetic/magnetoelastic induced martensitic transformation

The martensitic transformation is a diffusionless phase transition. The transition is between two different crystal structures that can be related by simple transformation operations⁵. Martensitic theory is extensive and well developed both theoretically and experimentally. One of the first modern treatments of the theory was published by Bowles and Mackenzie [27]. The literature is quite extensive, but two treatments that do an excellent job describing the theory and compiling experimental results are by Khachaturyan [28] and Nishiyama [29], respectively.

Without delving too deeply into the theory, there are some key concepts that need to be discussed. The martensitic transition (MT) transforms a parent phase called ‘austenite’ into a daughter phase called ‘martensite’. The transition is characterized by a starting temperature, M_S , and an ending temperature, M_F below which there is

⁵Operations such as rotation, expansion and contraction amount to an ‘invariant plane strain’ (for more information see appendix B).

no further transformation⁶.

Measurement of the martensite start and finish temperatures is commonly done by calorimetry. These temperatures can also be determined by measuring a wide array of material properties such as electrical resistivity, elastic modulus, and magnetic susceptibility. The reason for this is that the MT is a first order phase transition, and the thermodynamic potentials ($\frac{\partial \Phi}{\partial q}$) are discontinuous at phase transition temperatures. However, the effect of MT on the material properties is not always dramatic because the austenite phase does not instantaneously and completely transform into martensite.

The reason the austenite does not completely transform into martensite is because the elastic strain energy that controls the magnitude of the kinetic barrier can be quite large ($\sim 10^3 \text{ J/cm}^3$). This barrier is due to the volume mismatch between the austenite and martensite phase. In most cases the sample does not transform entirely into martensite but retains some of the parent phase⁷. This large energy barrier means that a large thermodynamic driving force (large undercooling, external stress, etc.) is necessary to initiate martensite formation and most samples do not transform fully to martensite. That is to say, there is always some amount of retained austenite.

The large strain energy associated with the transition leads to interesting and varied microstructures in the martensite. The martensite regions take the form of needles or plates.

Both regions can have a high density of dislocations, twins, stacking faults and other defects. The regions of martensite have a particular orientation with respect to the parent phase and this orientation plays an important role on the shape change and the resulting morphology of the sample that has undergone transformation.

⁶On heating, the temperature at the onset of austenite is called A_S and the transformation ends at a temperature A_F . $A_{S,F}$ are not, in general, equal to $M_{S,F}$ and this leads to a temperature hysteresis.

⁷It is important to note that while there is only a small difference in free energy between the phases, the kinetic barrier can be quite large simply because one phase must fit into another

The plate or needle morphology is a result of the interface between the parent and daughter phase having very low strain energy. Thus, a plate or needle, which has a high surface to volume ratio, is favored because the volume of the martensite phase has relatively high strain energy.

In some materials, the elastic barrier is quite low ($\leq 10 \text{ J/cm}^3$). In some special cases [11] the MT is completely reversible. Not only does the transition take place with a small value of $M_S - M_F$, but the macroscopic shape (and the microstructure) of the austenite is entirely recovered. This phenomenon is known as the shape memory effect (SME) and materials displaying the SME are called shape memory alloys (SMA). The SME is a very useful engineering concept, and much research has been done on developing SMA. The most successful SMA to date is equiatomic NiTi (also known by the trade name nitinol). NiTi shows almost perfect shape memory behavior along with a related phenomenon called superelasticity which will be covered later on in this section.

There are two subjects in martensitic transformation that are particularly relevant to this thesis.

- shape change, crystallography and microstructure resulting from MT
- the effect of an external forces (in the thermodynamic sense) on MT

2.2.1.1 shape change, crystallography and microstructure resulting from MT

One characteristic of martensitic transformations is the transformation proceeds in a minimum stress environment (ideally, zero stress). This means that the martensite phase fits into the austenite phase in the lowest stress configuration. Thus, in general the parent phase can be related to the daughter phase by a homogeneous distortion consisting of a distortion of the lattice combined with a rigid body rotation [30]. This particular deformation is known as an 'invariant plane strain'.

The following derivation is done from the microscopic point of view and as such is entirely correct when comparing one small region of austenite phase with the resulting martensite in that small region.

In the parent phase, a vector \vec{r} undergoes a transformation

$$\vec{r} \rightarrow \vec{r}'$$

If we represent the distortion by the matrix A_{ij} then

$$\vec{r}' = \hat{\mathbf{A}}\vec{r} \quad (2.11)$$

or

$$r'_i = A_{ij}r_j.$$

Now, to measure the strain in an arbitrary direction in the lattice, write down the displacement

$$\begin{aligned} \vec{u} &= \vec{r} - \vec{r}' = \vec{r} - \hat{\mathbf{A}}\vec{r} \\ &= (\hat{\mathbf{A}} - \hat{\mathbf{I}})\vec{r} \end{aligned} \quad (2.12)$$

where $\hat{\mathbf{I}}$ is the identity operator and the displacement operator U_{ij} is defined by

$$\vec{u} = \hat{\mathbf{U}}\vec{r} \quad (2.13)$$

$$u_i = U_{ij}r_j. \quad (2.14)$$

Thus the i th component of the strain is

$$\epsilon_i = \frac{u_i}{r_i} = \frac{1}{r_j} U_{ij}r_j \quad (2.15)$$

with the strain tensor defined as

$$\epsilon_{ij} \equiv A_{ij} - \delta_{ij} \quad (2.16)$$

Where δ_{ij} is the Kroeneker delta.

Similarly to the magnetoelastic tensor, when a material experiences a martensitic transformation, the deformation operator projected onto a specific lattice direction of the parent phase (see figure 2.6) gives the strain in that direction.

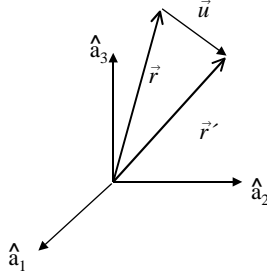


Figure 2.6: \vec{r} is transformed to \vec{r}' referenced in the \hat{a}_i coordinate system.

The operator $\hat{\mathbf{A}}$ is composed of a rigid body rotation⁸ and a lattice deformation resolved along a set of orthogonal axes (the principle lattice vectors).

Thus,

$$\hat{\mathbf{A}} = \hat{\mathbf{R}}\hat{\mathbf{F}}$$

where $\hat{\mathbf{R}}$ is a unitary matrix (also called a proper rotation). Because $\hat{\mathbf{F}}$ can be represented as distortions along orthogonal axes, it can always be diagonalized and because F_{ij} is real, $\hat{\mathbf{A}}$ is Hermitian.

Recall that the purpose of the previous derivation was to determine the distortion

⁸a rotation in which the relative positions of the rotated region remain unchanged

(the strain and the rotation) of the martensite phase relative to the austenite. So far only the strain has been solved for in terms of $\hat{\mathbf{A}}$. To get the rotation, Khachaturyan [28] shows that

$$\hat{\mathbf{F}}^2 = \hat{\mathbf{A}}^\dagger \hat{\mathbf{A}} \quad (2.17)$$

Thus the process of finding the rotation consists of four steps:

1. Take the product of $\hat{\mathbf{A}}^\dagger \hat{\mathbf{A}}$;
2. diagonalize $\hat{\mathbf{F}}^2$ to find the eigenvalues of $\hat{\mathbf{F}}$, λ_1^2 , λ_2^2 , and λ_3^2 .
3. This gives $\hat{\mathbf{F}}_{ii} = \lambda_i$ which can be used to find $\hat{\mathbf{F}}^{-1}$;
4. then $\hat{\mathbf{R}}$ can be found by $\hat{\mathbf{R}} = \hat{\mathbf{F}}^{-1} \hat{\mathbf{A}}$.

It is difficult to predict the value of $\hat{\mathbf{A}}$ a priori because the determination of the the parent and daughter phase is experimental by definition. Fortunately, the transformation itself is quite conducive to experimental observation, and as such there is a wealth of information for materials that undergo martensitic transformations. This information is then used to generate $\hat{\mathbf{A}}$. In chapter three $\hat{\mathbf{A}}$ will be explicitly solved and utilized for the case of the FCC→HCP transformation.

To illustrate the concepts discussed so far, consider figure 2.7. In this example a cubic lattice is transformed to a tetragonal phase. The parent phase is rotated about the \hat{a}_3 axis through an angle ϕ . The cube is elongated in the \hat{a}_3 direction and contracted along the \hat{a}_1 and \hat{a}_2 directions.

Therefore, the lattice deformation matrix is

$$\hat{\mathbf{F}} = \begin{pmatrix} \frac{b}{a} & 0 & 0 \\ 0 & \frac{b}{a} & 0 \\ 0 & 0 & \frac{c}{a} \end{pmatrix}$$

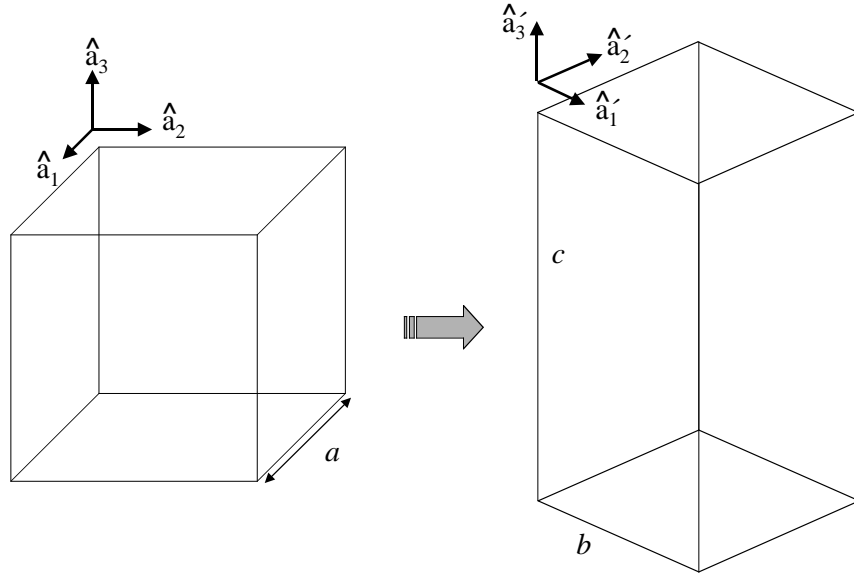


Figure 2.7: A cubic phase is transformed into a tetragonal phase by rotation around, and elongation of, \hat{a}_3 .

and the rotation matrix is

$$\hat{\mathbf{R}} = \begin{pmatrix} \cos \phi & \cos \phi - \frac{\pi}{2} & 0 \\ \cos \phi + \frac{\pi}{2} & \cos \phi & 0 \\ 0 & 0 & 1 \end{pmatrix}.$$

With the total distortion matrix

$$\hat{\mathbf{A}} = \hat{\mathbf{R}}\hat{\mathbf{F}} = \begin{pmatrix} \frac{b}{a} \cos \phi & \cos \phi - \frac{\pi}{2} & 0 \\ \cos \phi + \frac{\pi}{2} & \frac{b}{a} \cos \phi & 0 \\ 0 & 0 & \frac{c}{a} \end{pmatrix}.$$

As a demonstration, take the direction $[111]$. The strain in the $[111]$ direction is

transformed to

$$\hat{\mathbf{A}} \begin{pmatrix} 1 \\ 1 \\ 1 \end{pmatrix} = \begin{pmatrix} \frac{b}{a} \cos \phi + \cos \phi - \frac{\pi}{2} \\ \cos \phi + \frac{\pi}{2} + \frac{b}{a} \cos \phi \\ \frac{c}{a} \end{pmatrix}.$$

This gives the components of the new vector in terms of the parent coordinate system, that is,

$$\frac{1}{\sqrt{3}}(\hat{a}_1 + \hat{a}_2 + \hat{a}_3) \xrightarrow{\text{cubic to tetragonal}} \frac{1}{\sqrt{3}} \left((\hat{a}_1((b/a) \cos \phi + \cos \phi - \frac{\pi}{2}) + \hat{a}_2(\cos \phi + \frac{\pi}{2} + (b/a) \cos \phi) + \hat{a}_3(c/a)) \right).$$

The next important topic to discuss is the different orientations, or variants, that the martensite can form in the parent phase. This topic is important because it affects both microstructure and macroscopic shape change.

As mentioned in the beginning of the preceding derivation, $\hat{\mathbf{A}}$ correctly predicts the transformation on a microscopic scale. However $\hat{\mathbf{A}}$ does not predict the orientation of one region of martensite with respect to another.

It is observed that there can be numerous variants of martensite in a single sample whether the sample is polycrystalline or single crystal. This is because most crystal lattices have many symmetry elements or operations.

These symmetry operations allow for $\hat{\mathbf{A}}$ to operate simultaneously on crystallographical equivalent systems within the parent phase.

Using the previous example, the transformation proceeded about the \hat{a}_3 axis, but at another part of the sample it could have proceed along the \hat{a}_1 axis.

Khachaturyan [28] shows that for n symmetry operations of the parent phase there are n possible variants. If the symmetry element is $\hat{\mathbf{G}}$, then the deformation

operator is given by

$$\hat{\mathbf{A}}_n = \hat{\mathbf{G}}_n \hat{\mathbf{A}}_1 \hat{\mathbf{G}}^\dagger \quad (2.18)$$

where $\hat{\mathbf{A}}_1$ is the fundamental operator with respect to a chosen coordinate system in the parent phase.

When a sample is free of external forces it will form different martensite variants in order to minimize the total strain or shape change. External and internal stress, nucleation site density, and even the macroscopic shape of the sample can affect which variants are present.

In some materials external forces or specific geometry can be used to encourage only variants that give rise to a desired dimensional change. In this way a material like NiTi can be used as an actuator or a shape memory device.

2.2.1.2 effect of external forces on martensitic transition

The primary effect that a force⁹ has on a MT is to shift the martensite start (finish) temperature. It has been found that external forces have no effect on the kinetics of martensitic transformations [29] and only have an effect on the *amount* of austenite transformed (for a fixed temperature) by shifting the transition temperature so that the M_F is moved above or below the temperature of interest. This means that more or less undercooling (more or less austenite transformed) happens for a given temperature.

What one would like to do is to determine how an external force, such as stress, or changes in magnetization, affect the transformation temperature.

I will derive a generalized approach to determining the effect that a magnetic field has on an ideal system. Consider figure 2.8 where T_0 , M_S , and ΔF_M are the equilibrium temperature between the two phases, the temperature at which the trans-

⁹I use the term force in the thermodynamic sense. That is, the force is a conjugate to the geometric coordinate, q such that the force times the differential change in q is equal to the differential change in work. For a system subject to a n different forces, f_i , the work done through δq_i is $\delta W = \sum_{i=1}^n f_i \delta q_i$.

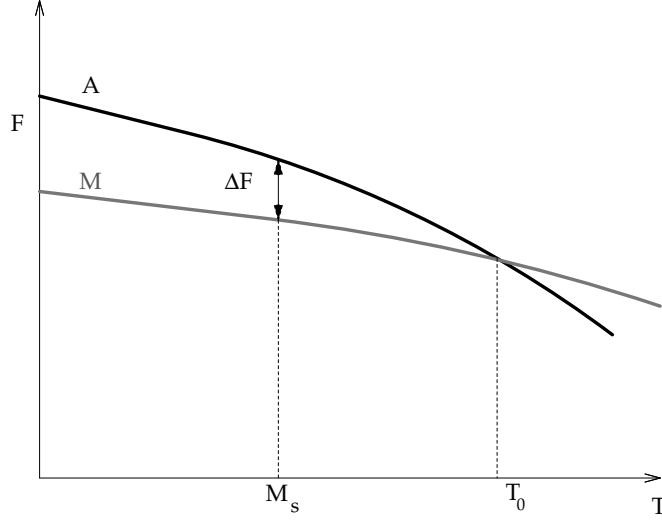


Figure 2.8: *The free energy curves of the martensitic (M) and austenitic (A) phases of a material undergoing a martensitic transformation*

formation begins, and the free energy (driving force) difference between the two phases at M_S respectively.

I assume that $T_0 \sim M_S$, or more appropriately $\frac{T_0 - M_S}{T_0} \ll 1$. Next, define a parameter t ,

$$t = T - T_0 \quad (2.19)$$

and expand the free energy about $T = T_0$,

$$F = F_0 + \frac{\partial F}{\partial t}t + \frac{\partial^2 F}{\partial t^2}t^2 \quad (2.20)$$

Given my previous assumption, $\frac{T_0 - M_S}{T_0} \ll 1$, F can be approximated as a linear function of t for small t . Thus, F has the form

$$F_{A,M} = \chi_{A,M}t + \delta \quad (2.21)$$

where A, M are for austenite and martensite, respectively, and obviously both curves have the same intercept. This model is shown in figure 2.9.

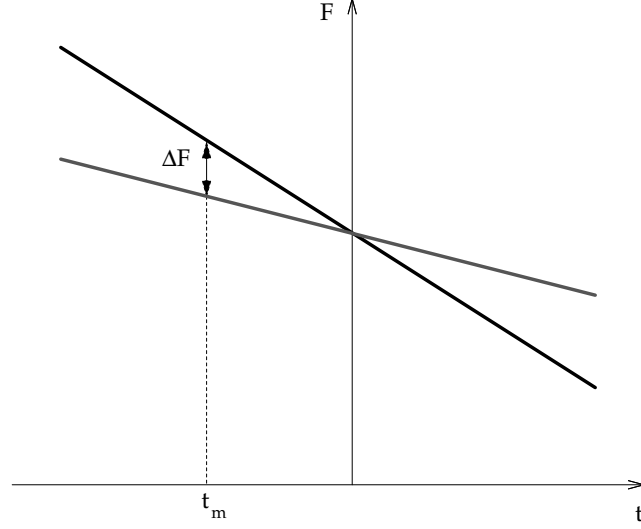


Figure 2.9: *The free energy of the system in figure 2.8 approximate as a linear function of the parameter t . ($t_m = M_S - T_0$)*

Next we apply an external force (such as a magnetic field) and assume that it has the effect of changing the difference in the free energy of the two phases by a constant amount (ΔE_M). This is represented in figure 2.10.

To find the change in the transformation temperatures, set $F_A = F_M$ so that

$$\chi_a t'_0 + \delta + \Delta E_M = \chi_m t'_0 + \delta \quad (2.22)$$

thus

$$t'_0 = \frac{\Delta E_M}{\chi_m - \chi_A} \quad (2.23)$$

and

$$\chi_M - \chi_A = \frac{F_M - \delta}{0 - t_M} - \frac{F_A - \delta}{0 - t_M} = \frac{\Delta F}{t_M}. \quad (2.24)$$

This can be worked out to give the new transformation temperature and the new martensite start temperature as

$$T'_0 = \frac{\Delta E_M}{\Delta F} (M_S - T_0) + T_0 \quad (2.25)$$

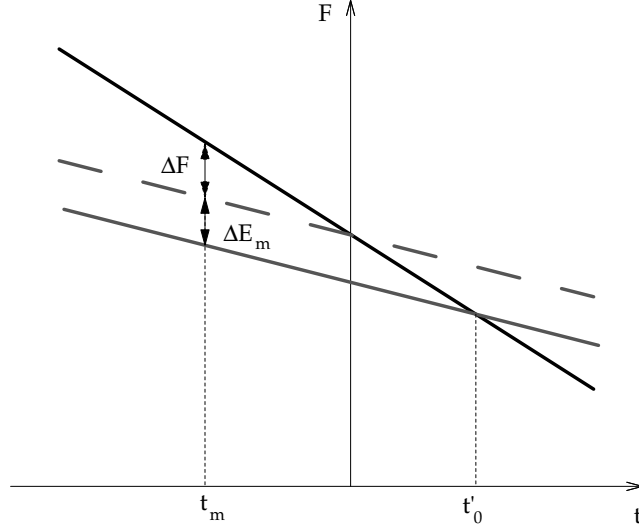


Figure 2.10: *Change in free energy due to an external force.*

and

$$M'_s = \frac{\Delta E_M}{\Delta F} (T_0 - M_S) + M_S \quad (2.26)$$

These expressions encourage the following relation,

$$\frac{\Delta E_M}{\Delta F} = \frac{T'_0 - T_0}{M_S - T_0} = \frac{\left(\frac{T'_0}{T_0}\right) - 1}{\left(\frac{M_S}{T_0}\right) - 1} \quad (2.27)$$

Since M_S is always less than T_0 the sign of equation 2.27 tells you the effect of the external force on the free energy, that is to say, whether the external force moves the free energy of the phases closer together or further apart.

2.2.2 deformation through twin boundary motion

Twin boundary motion (TBM) is a mechanism for large deformation in materials with a twinned microstructure. TBM is observed to occur by changes in twin variants— either through rearrangement of the existing twin structure or by growing one favorable variant at the expense of the others¹⁰.

¹⁰similar to the case of domain magnetization

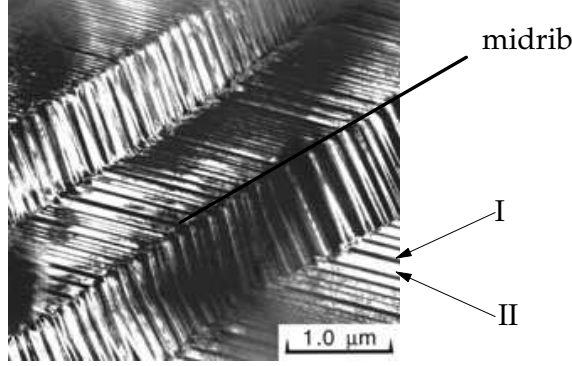


Figure 2.11: *The twin microstructure in Nb-Ru. I and II refer to the two twin variants (the light and dark regions). The midrib is not a twin boundary, but divides two regions that have the same twin variants but different orientation relative to the parent phase.*

Twin boundary motion takes place in response to a change in free energy of the sample due to an external force, for example, due to an external stress or change in state in magnetization. If the sample recovers its shape when the driving force is removed, the term reversible twin boundary motion (RTBM) is used.

RTBM is only observed in materials that undergo a martensitic transformation in which the twinned microstructure is found. Before the phenomenon of RTBM is reviewed, it is important to review the concept of the twin microstructure

2.2.2.1 the twin microstructure

Figure 2.11 shows the twinned microstructure in a Nb-Ru alloy [29]. In martensitic samples the specific twin variants depend on the crystal structure, whereas the microscopic (or mesoscopic) structure depends on both the external conditions of the sample and the preexisting microstructure of the parent phase.

The twin microstructure is a way for a material to reduce strain energy, and as such, it is seen in many materials. This reduction of strain energy is why the twinned microstructure is so common in martensitic materials where strain energy plays such an important role. There are other competing mechanisms to reduce strain energy in the martensite/austenite system; however, dislocation and stacking faults are the two

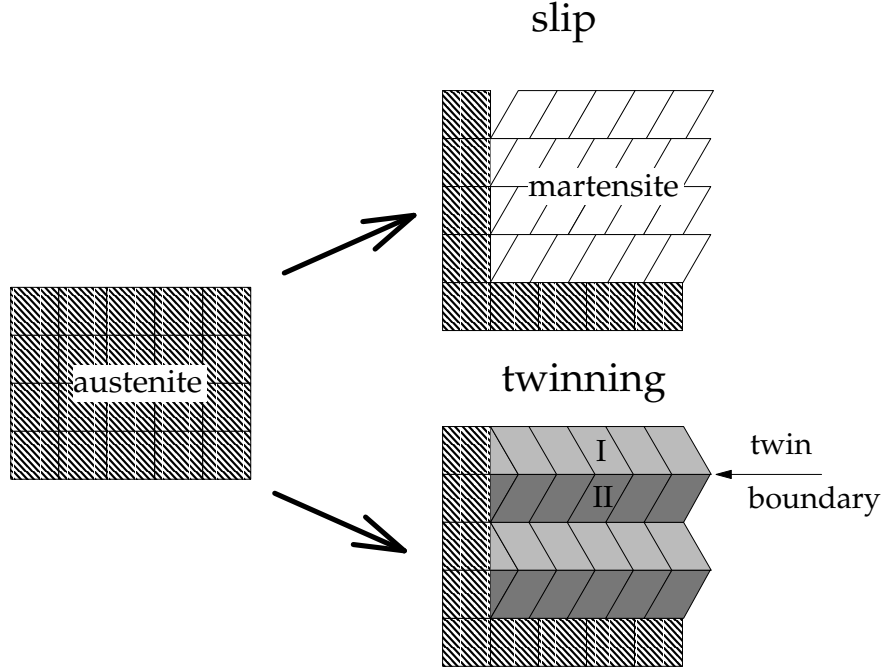


Figure 2.12: *Two extreme examples of microstructure resulting from martensitic transformation. The top structure results from accommodation solely by slip, the bottom structure results from twinning. I and II refer to the different twin variants.*

most important. Figure 2.12 shows a schematic of the difference between twin and slip in accommodating martensite. In general, both twins and dislocation networks are observed in materials that have undergone a martensitic transformation.

Two twins can be geometrically related to each-other either by any operation of macroscopic symmetry (reflection, proper rotation, or inversion) [31]. The *twin boundary* is the planar region separating the two twins. The *twin plane* is the plane in which the twin can be observed. The twin plane normal lies in the twin boundary plane. The twin plane is perpendicular to the mirror plane in case of twin relation by reflection, and the twin plane normal is parallel to the axis of rotation in the case of rotation.

It is well known that mechanical shear can lead to twin formation [14] even in materials that do not exhibit the martensitic transformation. This lends some plausibility to the notion that twin motion and growth occurs in deformed martensite

materials because twins are seen to be somewhat dynamic structures.

2.2.3 reversible twin boundary motion

RTBM is seen in many different materials [11], but the term pseudoelasticity is more commonly used in order to convey a sense of what is of interest in the system at hand. In different materials that exhibit RTBM, the term used to describe the pseudoelastic behavior are descriptive of the physical processes that stimulate RTBM.

The following three examples, superelasticity, rubber-like behavior, and the ferromagnetic shape memory effect (FSME), have very different circumstances but all display pseudoelasticity through RTBM.

2.2.3.1 superelasticity

Superelasticity is seen, most notably, in Ni-Ti alloys [11] around the equiatomic composition range. Figure 2.13 shows a schematic stress-temperature 'phase' diagram. This non-equilibrium diagram shows different regions where austenite or martensite is stable. The regions are bounded by the stability of the system with respect to slip, martensite formation, and twin boundary motion.

In this case, the alloy is selected so that the operating temperature is well above M_s . When a stress is applied, the material forms what is called thermoelastic martensite [11]. This martensite has a twinned microstructure determined by the direction of the applied stress. Upon further increase in stress the materials undergoes twin boundary motion. When the stress is removed the sample reverts first to its original twin structure and then to the austenite. The driving force for this is due to the fact that the deformation is done under conditions in which the austenite phase is stable with respect to the martensite. This process is illustrated in figure 2.14. Recoverable strains as large as 10 percent have been measured [11].

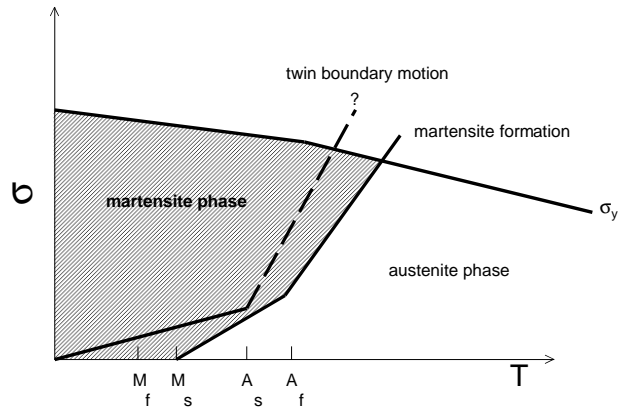


Figure 2.13: *Stress vs temperature for Ni-Ti or similar materials. The line indicating twin boundary motion is suggestive of the where twin boundary motion is stable with respect to the formation of martensite.*

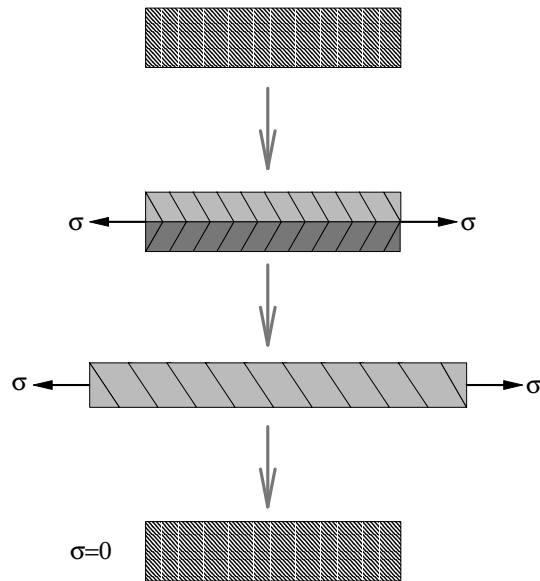


Figure 2.14: *Tensile deformation of a super elastic material. The sample starts in the undeformed austenite phase, then converts to martensite with two twin variants. Further stress leads to a single twin variant. When the stress is removed the sample returns to its original austenite shape.*

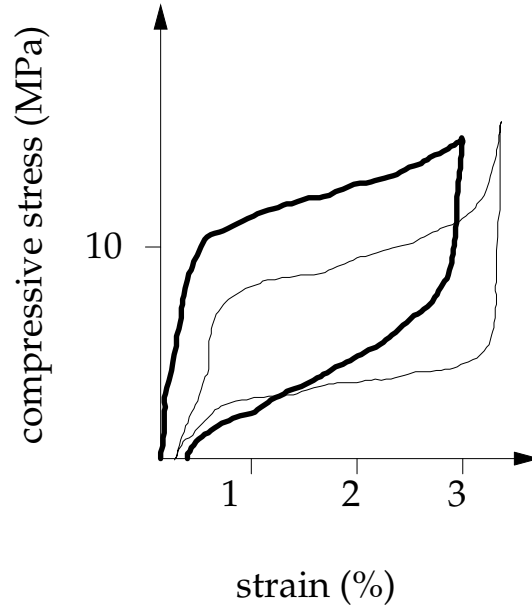


Figure 2.15: *Pseudoelastic behavior in $\text{Au}_{51}\text{Cd}_{49}$ reported in [13]. The heavy line is for the first deformation cycle. The light line is for the third cycle (additional cycles showed similar behavior). The strain rate was $\sim 10^{-2}/\text{s}$.*

2.2.3.2 'rubberlike' behavior

Sakamoto and Ren [13, 12] describe RTBM in Cu-Ni-Al and Au-Cd alloys. In this case, the samples are prepared by placing them in tension at temperatures well above A_F and then cooling them below M_F while in tension. This results in a specimen that has two twin variants with a specific relationship to the tensile axis. Upon application of compressive stress the samples exhibited the behavior shown in figure 2.15. For tensile stress, the same behavior was reported, but at stresses five- times greater and one-third the strain.

The authors use the term "rubber-like behavior" to describe the pseudoelastic response in these materials. Ren [12] proposed the driving force for reversal of twin motion involves short range order of atoms on two different sublattices. This is partially based on the observation that rubberlike behavior was only seen in samples that had been aged at $T < M_F$ for a period of months.

The explanation is as follows: The austenite consists of two sublattices that are

disordered. When the sample transforms into martensite a partial short-range ordering takes place in the sublattices. When the sample is distorted by twin motion this affects the local ordering by distorting the lattices. This disruption of short-range order is suggested to be responsible for the RTBM observed.

2.2.3.3 FSME

Recently RTBM has been reported in Ni-Mn-Ga and Fe-Pd-Pt alloys. This is the so-called¹¹ ferromagnetic shape memory effect (FSME). It is unique to the previous two examples because there is no external stress involved.

Udalako [20] and others originally reported strains of about 0.2% in NiMnGa. More recently Murray [15] reported a reversible shear strain of 7% in Ni₂MnGa, while Kakeshita [19] has reported 0.5% reversible strain in ordered Fe₃Pt. In all cases reversible twin boundary motion has been observed and credited as the mechanism responsible for the large strains. All measurements were done at temperature below M_F .

The proposed mechanism [21] for these large 'magnetostrictive' strains is as follows. When a magnetic field is applied, one twin variant has lower magnetocrystalline anisotropy energy¹² than the other. For a material with a large enough magnetocrystalline anisotropy, it is energetically favorable for the twin with higher magnetocrystalline anisotropy energy to convert to the other twin variant by twin boundary motion.

A final comment about the FSME. Researchers have not postulated a driving force for the *reversal* of twin boundary motion, even though it is observed that the strain state goes to zero when the field is reduced to zero. It is not clear if the sample is demagnetized when the field is turned off. If, as some suggest, the elastic strain drives the reverse transformation, then the reduction in strain energy would have to

¹¹the materials are ferromagnetic and exhibit analogous behavior to shape memory alloys

¹²i.e. the easy magnetic axis of the favorable twin variant lies parallel to the applied field

overcome the increase in magnetocrystalline anisotropy energy if the sample was to stay magnetized.

Of the three examples discussed, only the superelastic case has been observed in polycrystalline materials. Both rubberlike behavior and the FSME have only been observed in single crystal samples. One possible explanation is that, for polycrystalline samples, these effects are greatly reduced due to the constraint of randomly oriented grains. Alternatively, the Ni-Ti system could be a special case in which a polycrystalline material can exhibit pseudoelasticity.

2.3 summary

Because so many different concepts have been discussed, it is worthwhile to integrate the ideas in this chapter in terms of magnetostriction. Magnetostriction refers to the observation of strain or shape change due to an applied magnetic field. The first concept discussed was the semi-classical derivation of the magnetoelastic effect. Because magnetoelastic strains are very small, they provide a good lower bound on what is to be expected from a material.

Non-magnetoelastic terms discussed above include martensitic transformations and the related concept of pseudoelasticity. Martensitic transformation provides the possibility of magnetostriction via the contribution of magnetostatic energy, which can change the driving force for martensite formation. Pseudoelasticity is tied to magnetization through the FSME. However, the contributions of magnetoelastic energy, magnetostatic energy, and magnetocrystalline anisotropy all have to be considered in driving phase transitions and reversible twin boundary motion.

In the next chapter I will account for all of these terms in the Co-Ni alloy system. A theoretical model will be developed to approximate the magnitude of possible magnetoelastic contributions. Even though no data exists for the alloy range being

investigated, the system is simple enough to justify extrapolation of general theory.

Ultimately, the materials will have to be measured, and the magnitude of the magnetostrictive response will serve as a guide as to which mechanisms are present.

Chapter 3

Special Considerations in the Co-Ni Alloy System

Chapter 2 described the phenomenon of magnetostriction and gave a way of calculating the strain. Now those formulae can be applied to the Co-Ni alloy system and in particular to thin films. Because the magnetoelastic constants have not been determined for the Co-Ni alloy ranges I am testing, I will use the values of cobalt and nickel that have been compiled and then try to extrapolate based on the crystallography of the sample (i.e. whether it is in the cubic, hexagonal, or mixed phase). This approach should give a lower and upper bound for magnetostrictive values.

In chapter 5 the experimental values of the magnetoelastic coefficients for Co-Ni alloys I have tested will be compared to the following predicted values.

Whereas there is no magnetoelastic data for cobalt rich Co-Ni alloys, there is considerable¹ thermodynamic, structural, phase transformation, and magnetic data for thin film and bulk Co-Ni alloys [32, 33, 34, 35, 36, 37]. This data will allow for a more confident prediction of the forces involved for twin boundary motion and the martensitic phase transition.

¹most data tends to concentrate on alloys with greater than 50% Ni

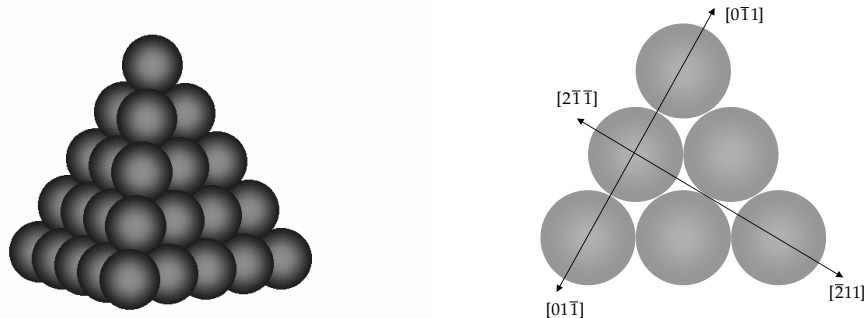
3.1 crystallography of Co-Ni thin films

Before the values of magnetostrictive strain can be calculated for the samples at hand, the crystallography must be described. Since the Co-Ni system is close-packed, the crystallography is relatively simple. Close-packed layers (either $\{111\}$ oriented for FCC samples or $\{0001\}$ for hexagonal) grow parallel to the substrate. Because the films are grown on silicon nitride, which is amorphous, they are polycrystalline with a grain size comparable to the film thickness. The grains are randomly oriented in the film plane.

In order to calculate the magnetostriction in these films one must have an understanding of the relationship between grain orientation and the principle (crystal) axes. For the hexagonal phase, this is simple. Chapter 4 includes x-ray and electron diffraction data which show the hexagonal phase to be oriented with the c axis normal to the film. Since hexagonal materials are isotropic in-plane the average magnetostriction at various orientations (relative to the film geometry) can be calculated in a straightforward manner using equation 2.10.

The cubic phase is more complicated because the grains are $\langle 111 \rangle$ oriented which is not one of the principle axes. This means an average 'in-plane' direction must be determined by symmetry or a statistical calculation. In order to proceed with the calculation of the magnetostriction in the cubic phase it is instructive to consider what the close packed structure for FCC materials looks like in terms of principle directions and planes.

A handy model for understanding the FCC lattice is the Thompson tetrahedron. This is a real-space construction, and while it does not show the cubic nature of FCC materials, it is very effective at illustrating geometrical relations for the close-packed faces. The Thompson construction is composed of the four intersecting $\{111\}$ planes. The construction gives crystallographic information that is more useful for real FCC materials. This is due to the fact that FCC materials tend to form with the close-



(a) *The real-space construction of the Thompson tetrahedron (note that the fundamental construction is only three layers).*

(b) *The (111) face with the two crystallographically different directions.*

Figure 3.1: *The Thompson tetrahedron construction for FCC crystals*

packed planes bounding the solid [38]. Figure 3.1 shows the Thompson tetrahedron (constructed from individual atoms) with a detailed view of the (111) face.

3.2 magnetoelastic contributions to magnetostriction for a Co-Ni thin film

In chapter four x-ray diffraction data is shown for different films. For films with greater than 20% weight Ni, grown on silicon nitride, it is found that the films are a mixture of $\langle 111 \rangle$ and $\langle 100 \rangle$ textures. That is to say, the film normal is parallel to $\langle 111 \rangle$ or $\langle 100 \rangle$ axes of the film grains.

For films less than 20% weight Ni, all grains are oriented with the close-packed direction parallel to the film normal. However these films have a mix of cubic and hexagonal grains. Figure 3.2 shows an example for cubic grains. The in-plane orientation is random, but the texture is $\langle 111 \rangle$.

In looking at the strain-magnetization relationship there are two cases to consider for each phase: In-plane and perpendicular magnetization with strain measured

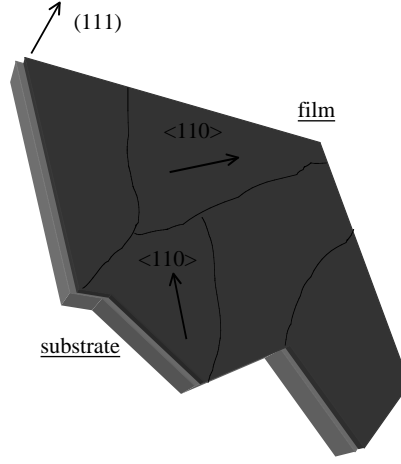


Figure 3.2: *Typical configuration of Co-Ni thin films. The individual grains are all oriented with the close packed direction normal to the film plane. The in-plane orientation is random.*

in-plane. These conditions are important because they represent an upper and lower bound on in-plane magnetostriction. In addition, these two cases can be solved analytically and thus serve to illustrate the general idea of calculating magnetostriction.

3.2.1 $\langle 111 \rangle$ oriented cubic grains

3.2.1.1 magnetized in-plane, strain measured in plane

To get the value² of λ_{ip}^{ip} one must account for the fact that the grains have random orientation in plane so the average in-plane magnetization direction is an average of all possible $\langle 110 \rangle$ and $\langle 112 \rangle$ directions. In principle this is a non-trivial calculation that has to be carried out by statistical averaging over all grains, but for the case of magnetostriction the symmetry of the film and the symmetry of the magnetostrictive terms can be taken advantage of.

²in the following calculations the upper index is for the direction of magnetization, the lower index for the strain measuring direction

No matter how an individual grain is oriented, it will never be more than 30 degrees away from a $\langle 112 \rangle$ or $\langle 110 \rangle$ direction. Thus, a good approximation to the direction of magnetization relative to any grain is the normalized vector average of these two directions. To calculate the average direction, a specific $\{111\}$ plane must be used. Choosing the (111) plane, we see the 12 possible average directions gives a result of the type

$$\langle 2\bar{1}\bar{1} \rangle + \langle 10\bar{1} \rangle = \langle 3\bar{1}\bar{2} \rangle . \quad (3.1)$$

Of course, if one averaged over all these vectors, the result would be zero. However recalling equation 2.5 and rewriting it as

$$\lambda = \frac{3}{2}\lambda_{100} \sum_i (\alpha_i^2 \beta_i^2 - \frac{1}{9}) + 3\lambda_{111} \sum_{i \neq j} \alpha_i \beta_i \alpha_j \beta_j \quad (3.2)$$

when $\alpha_i = \beta_i$ it is obvious that simply permuting the sign and value of the components of $\langle 123 \rangle$ does not change the value of λ . So, in terms of the magnetostriction, it does not matter what in-plane orientation an individual grain has. If the film is oriented $\langle 111 \rangle$, it is sufficient to specify the in-plane direction as one of the vectors in equation 3.1.

The physical reason for this is simply that the strain is invariant under 180 degree rotations ($e_{xy} = e_{yx}$). It is also important to note that it is assumed each grain is free to strain in the direction of magnetization. That is, all the grains strain in a cooperative manner. This is not too bad of an assumption based on the geometrical arguments made in this section and the fact that the grain boundaries and the substrate constrain each grain isotropically for small strains. In any case, this provides an upper bound on the calculation of magnetostrictive strain.

To calculate the in-plane strain with parallel magnetization use

$$\begin{aligned}\frac{1}{\sqrt{14}}[12\bar{3}][100] &= \alpha_1 = \beta_1 = \frac{1}{\sqrt{14}} \\ \frac{1}{\sqrt{14}}[12\bar{3}][010] &= \alpha_2 = \beta_2 = \frac{2}{\sqrt{14}} \\ \frac{1}{\sqrt{14}}[12\bar{3}][001] &= \alpha_3 = \beta_3 = -\frac{3}{\sqrt{14}}\end{aligned}$$

for example. From equation 2.5

$$\lambda_{ip}^{ip} = \frac{1}{4}\lambda_{100} + \frac{3}{4}\lambda_{111}. \quad (3.3)$$

All the alloys tested in this thesis have high cobalt content (≥ 70 weight percent cobalt); so it is not unreasonable to use the material values for cobalt to evaluate an upper bound on λ_{ip}^{ip} . Using the values of λ_{100} and λ_{111} from table 2.1 gives

$$\lambda_{ip}^{ip} = 7 \times 10^{-5}.$$

3.2.1.2 $\langle 111 \rangle$ textured film magnetized perpendicular, strain measured parallel

In this case all of the $\langle 123 \rangle$ type vectors are equivalent because $\alpha_i = \frac{1}{\sqrt{3}}$ and thus the term

$$\sum_{i \neq j} \alpha_i \alpha_j \beta_i \beta_j$$

is always equal to

$$-\frac{1}{3}\left(\frac{7}{14}\right) = -\frac{1}{6}$$

Thus

$$\lambda_{perp}^{ip} = -\frac{1}{6}\lambda_{111} = -2 \times 10^{-5}. \quad (3.4)$$

again, using the magnetostriction data for cubic cobalt. It is interesting to note that the that the strain in the film changes from compressive, for the in-plane condition, to tensile in the perpendicular condition.

3.2.2 <100> oriented cubic grains

As in the case of the <111> oriented grains, one can arrive at an expression for the average in plane direction for the <100> grains. By inspection, this direction is <110>. Thus, for the case of in-plane magnetization and in-plane strain measurement, we get the result from chapter two, namely

$$\begin{aligned}\lambda_{110} &= \frac{1}{4}\lambda_{100} + \frac{3}{4}\lambda_{111} \\ \lambda_{ip}^{ip} &= 7 \times 10^{-5}.\end{aligned}\tag{3.5}$$

This is the exactly same value as for the <111> oriented grains. Thus, for cubic films, a mixed texture has no effect on the theoretical value of in-plane magnetostriction due to in-plane magnetization.

For the perpendicular case, the in-plane magnetostriction is,

$$\begin{aligned}\alpha_1 &= 1; \alpha_2 = \alpha_3 = 0 \\ \beta_1 &= \beta_2 = \frac{1}{\sqrt{2}} \\ \lambda_{ip}^{perp} &= -\frac{B_1}{(c_{11} - c_{12})}\left(1 - \frac{1}{3}\right) = \lambda_{100}^{cobalt} = 7.5 \times 10^{-5}\end{aligned}\tag{3.6}$$

3.2.3 hexagonal phase magnetostriction

Figure 3.3 shows the hexagonal phase geometry of the thin films. The films have grains oriented with the [001] axis normal to the film. An in-plane magnetization for the randomly oriented grains takes the average value of [110].

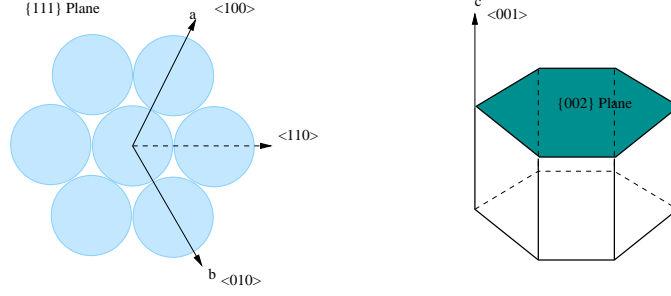


Figure 3.3: *For the hexagonal phase note that the average value of the in-plane (basal plane) direction is $\langle 110 \rangle$. Also, the form of the magnetostriction is symmetric with respect to \hat{a} and \hat{b} lattice directions.*

Equation 2.10 gives the in-plane strain as

$$\begin{aligned} \frac{\partial l}{l} = & \lambda_A [(\alpha_1 \beta_1 + \alpha_2 \beta_2)^2 - (\alpha_1 \beta_1 + \alpha_2 \beta_2) \alpha_3 \beta_3] \\ & + \lambda_B [(1 - \alpha_3^2)(1 - \beta_3^2) - (\alpha_1 \beta_1 + \alpha_2 \beta_2)^2] \\ & + \lambda_C [(1 - \alpha_3^2) \beta_3^2 - (\alpha_1 \beta_1 + \alpha_2 \beta_2) \alpha_3 \beta_3] \\ & + 4\lambda_D (\alpha_1 \beta_1 + \alpha_2 \beta_2) \alpha_3 \beta_3 \end{aligned}$$

With

$$\begin{aligned} \alpha_1 = \alpha_2 = \beta_1 = \beta_2 &= \frac{1}{\sqrt{2}} \\ \alpha_3 = \beta_3 &= 0 \end{aligned}$$

all terms involving α_3 and β_3 are eliminated, thus the hexagonal in-plane strain is (using cobalt data)

$$\lambda_{ip}^{ip,hex} = \lambda_A = 4.5 \times 10^{-5}. \quad (3.7)$$

The perpendicular condition has

$$\begin{aligned} \alpha_1 = \alpha_2 &= 0; \quad \alpha_3 = 1 \\ \beta_1 = \beta_2 &= \frac{1}{\sqrt{2}}; \quad \beta_3 = 0. \end{aligned}$$

Upon inspection of equation 2.10 each coefficient of λ_i is zero, and therefore the in-plane strain for hexagonal grains is zero when magnetized out-of-plane.

3.3 non-elastic contributions to magnetostriction in Co-Ni

Determining the shape change due to FCC to HCP transformation is much simpler than determining the magnetoelastic contribution. Theoretically the transformation proceeds very simply as a partial dislocation of $\frac{a}{6} \langle 112 \rangle$ (where a is the cube edge length in the cubic phase) every third layer. There are four equivalent close-packed faces that this transformation can proceed on, and three equivalent directions for layers to move, making 12 equivalent slip systems. The resulting shear displacement is approximately 19 degrees for a transformation proceeding on only one slip system. This process of activating slip systems is called 'shuffling'.

In addition to the shear displacement of close-packed layers, in cobalt alloys (among others) the sample will contract in the $\langle 111 \rangle_{\text{FCC}}$ ($\langle 001 \rangle_{\text{HCP}}$) direction and expand isotropically in the basal plane of the hexagonal system.

In unconstrained samples with an isotropic bulk shape there is no net shape change due to equal transformation on all 12 slip systems, thus all shape change is due to the isotropic contraction and expansion. Khachaturyan [28] derives the deformation matrix in cobalt by neglecting the shuffling and considering an isotropic strain in the basal plane (of the hexagonal system) together with a strain in the close-packed direction. Thus, the strain/deformation matrix is

$$u_{ij} = -0.00185 \begin{pmatrix} 1 & 0 & 0 \\ 0 & 1 & 0 \\ 0 & 0 & 1 \end{pmatrix} - 0.00607 \begin{pmatrix} \frac{1}{3} & \frac{1}{3} & \frac{1}{3} \\ \frac{1}{3} & \frac{1}{3} & \frac{1}{3} \\ \frac{1}{3} & \frac{1}{3} & \frac{1}{3} \end{pmatrix} \quad (3.8)$$

| deformation mechanism | strain contribution |
|--------------------------|---------------------|
| magnetoelasticity | $10^{-4} - 10^{-6}$ |
| FCC to HCP (homogeneous) | 10^{-3} |
| FCC to HCP (shuffling) | 19 % shear strain |

Table 3.1: *Estimated maximum in-plane strain contributions for a textured Co-Ni thin film.*

and since

$$A_{ij} = \delta_{ij} + u_{ij} \quad (3.9)$$

we get the lattice transformation matrix as

$$A_{ij}^{Co} = \begin{pmatrix} 0.9961 & -0.002 & -0.002 \\ -0.002 & 0.9961 & -0.002 \\ -0.002 & -0.002 & 0.9961 \end{pmatrix}. \quad (3.10)$$

So, for example, operating on the $\langle 110 \rangle$ family of directions in the HCP phase gives an expansion of $\sim 10^{-3}$.

3.4 summary

To conclude this chapter, it is useful to compare the contributions to the total deformation in a Co-Ni film. While it is difficult to predict what mechanisms and what values of magnetostriction will be found in the Co-Ni films, examining table 3.1 gives a way to evaluate an upper bound on the mechanisms of magnetostriction.

For example, if a sample shows a magnetostrictive strain of 10^{-3} , it is clear that a non-magnetoelastic mechanism is responsible. On the other hand, if a strain of only 10^{-5} is found it doesn't necessarily rule out non-magnetoelastic mechanisms. However, if a strain of 10^{-7} is found, it is most likely that magnetoelasticity is solely

responsible.

Chapter 4

Experimental Procedure and Material Analysis

In determining the optimal Co-Ni alloy for magnetostrictive applications the structural and magnetic properties of the sample as well as the magnetoelastic constants must be carefully measured.

Initially, the work in this thesis included a temperature dependent magnetostriction measurement. However, because these materials are expected to be operated at room temperature, it was decided that it is more practical to investigate as wide a range of compositions as possible instead of focusing on the 30-33 wt% Ni alloys that have been found to work at low temperatures (200 K).

This chapter will cover thin-film preparation techniques as well as magnetic, structural properties. Magnetoelastic characterization techniques will be discussed in chapter 5. For general reference, table 4.1 summarizes the films grown for this thesis. Alloy sources were 10, 15, 20, and 30 percent by weight nickel¹.

¹When the films grown from these alloys are referred to in the thesis, the notation 15%, 20%, etc. will be used even though that is not the exact composition of the film.

| composition ^a | annealing temperatures technique | thickness |
|--------------------------|-------------------------------------|----------------------------------|
| 12 wt.% Ni | 450 °C | 50 nm, 500 nm |
| 16 wt.% Ni | 450 °C | 50 nm, 500 nm |
| 21 wt.% Ni | 450 °C , 600 °C | 50 nm, 300, 500 nm |
| 32 wt.% Ni | 450 °C , 550 °C , 600 °C , 700C | 50 nm, 200 nm, 400 nm, 500 nm |

Table 4.1: *Summary of various Co-Ni films grown for this study*

^aas determined by EDX

4.1 thin-film preparation

Alloy films can be prepared in a number of ways on various substrates. The goal of this thesis is to examine polycrystalline films on amorphous substrates. Also of interest is to examine the magnetostrictive properties as a function of thickness². Thin-films were grown by evaporation up to a thickness of 0.5 μm .

4.1.1 substrate selection

Both silicon nitride and silicon oxide were used. These substrates are readily available for thin film deposition, and both Si_xN and SiO_2 are common passivation layers in microelectronic and MEMS devices. Thus, the results of this thesis can be immediately transferred to those technologies.

A titanium 'glue layer' was used for some films to improve adhesion of the metal films. Titanium is very reactive with oxides and nitrides as well as metal films— this makes titanium a good intermediate layer. However, care must be taken not to poison the Co-Ni films, this means the titanium layer is less than one percent the thickness of the metal film.

²Thickness dependence is used to study how, and if, a thin-film differs from bulk like behavior—by increasing the thickness the film becomes more bulk-like.

4.1.2 heat treatment

Heat treatment (annealing) was used to control the microstructure of the thin-films—in particular the grain size and in-plane texture (as described below).

Typical annealing temperatures ranged from 450 °C to 700 °C . Annealing was done both post growth (in situ for evaporated films) and during deposition. Heat treatment times were typically on the order of 10 ks. The range of grain size is more or less constant, ranging from about 20 nm to 1000 nm, for all temperatures for the evaporated films. However, higher temperatures provide better adhesion and increased average grain size.

4.1.3 film growth

Thin films were prepared by evaporating from an alloy source (congruent evaporation) and by evaporating thin alternating layers of cobalt and nickel and then interdiffusing them by heat treatment—this method allows for excellent control of stoichiometry.

The second method, which has been used for other thin-films [39], was abandoned because in order for thorough interdiffusion to take place, the layers must be less than 1 nm thick. This makes it an impractical technique for growing films much thicker than 50 nm.

Congruent evaporation became the method of choice because cobalt and nickel have very similar vapor pressures in the range of melting temperatures for all compositions chosen. The ratio of fluxes from an A_xB binary alloy source is [40]

$$\frac{J_{vA}}{J_{vB}} = \frac{x}{1-x} \frac{p_{vA}}{p_{vB}} \sqrt{\frac{M_B}{M_A}} \quad (4.1)$$

Where p_v is the vapor pressure and M is the molecular mass. Because the molecular mass of cobalt and nickel differs by less than 0.1 percent, if the vapor pressure is the same at the temperature of interest the flux ratio will be the same as the source

composition.

4.1.4 microstructure and composition

The microstructure of the films was remarkably similar to that of the bulk. The difference being one of scale. Figure 4.1 show an optical micrograph of a 25 wt% Ni alloy. This sample was prepared by vacuum melting the alloy into a button. Then, the sample was sectioned, ground, polished to 0.3 μm grit, annealed, and then etched in *aqua regia*.

As discussed in chapter three, the morphology of this sample will show transformation on the equivalent $\{111\}$ planes. Thus, in figure 4.1 the triangular shapes are due to a transformation in a grain that is nearly aligned with the surface. If the surface and a $\{111\}$ plane were perfectly aligned the triangles would be perfect equilateral triangles.

Figure 4.2 shows a TEM of a Co: 30 wt% Ni film. This grain displays the same morphology as the bulk, but at a scale three order of magnitude smaller.

The gross grain structure of the film did not vary much with thickness or annealing conditions (above 450 $^{\circ}\text{C}$). The films grew in what is referred to as 'zone 2' (or Z2) [40]. Z2 is characterized by textured grains with a distribution of sizes on the order of, and less than, the film thickness. However, for films annealed at 650 $^{\circ}\text{C}$ or higher, the films were still textured, but the upper limit of the grain size increased to well beyond the thickness of the film. Figure 4.3 shows a TEM of the same film as in figure 4.2 but at lower magnification; so the overall grain size distribution is emphasized.

The similarity of the composition of the thin-films to the bulk source was confirmed by energy dispersive x-ray analysis (EDX). It was found that the thin-films differed from the source by no more than a two percent, well within the experimental uncertainty of the measurement technique. Auger analysis would provide a more accurate measurement of the composition but only for a small fraction of the film

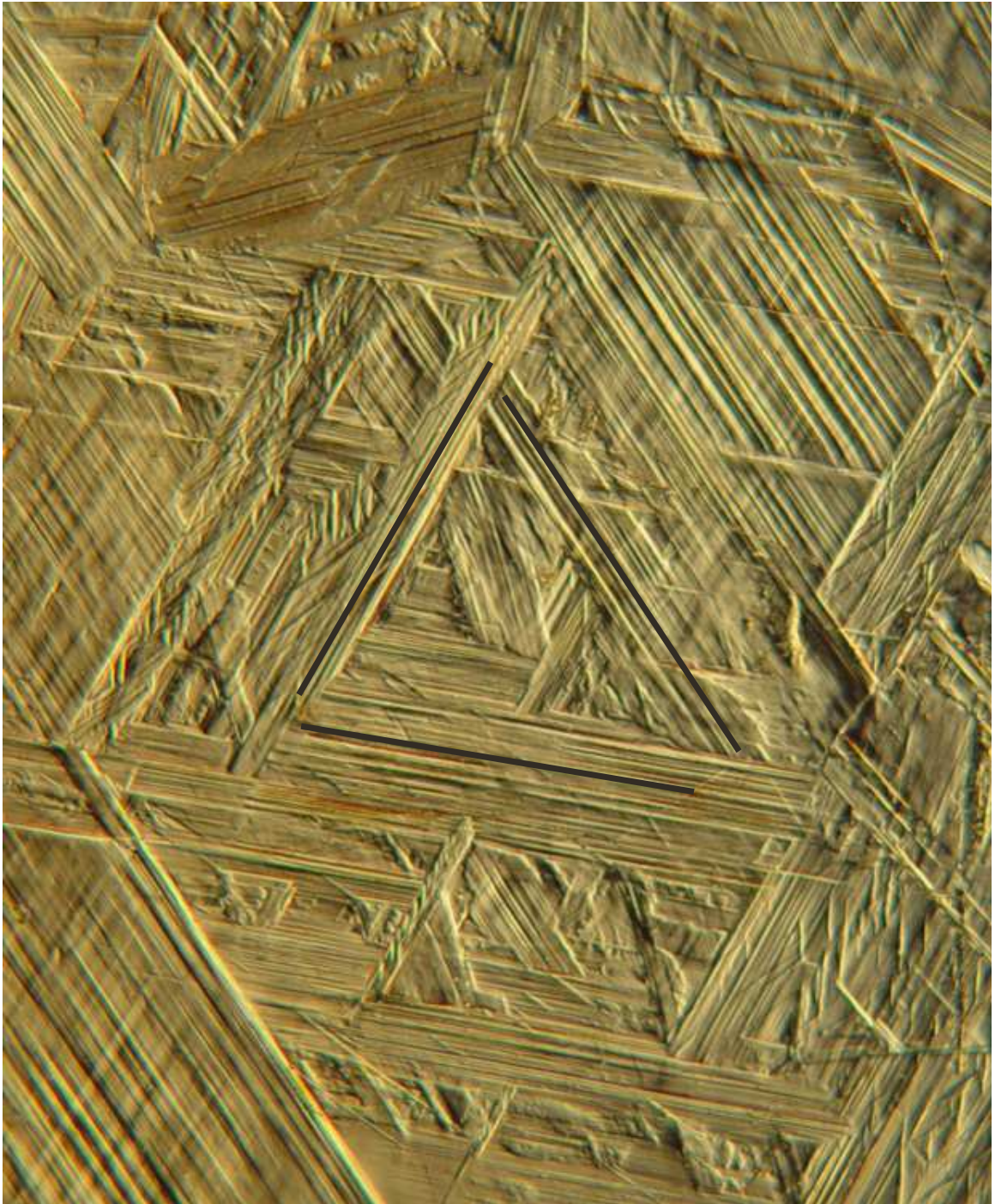


Figure 4.1: A single grain of Co: 25 wt% Ni, annealed at 450 °C for 12 hours. The HCP phase is present as the heavily twinned regions. The heavy black lines mark three equivalent $\{111\}$ variants, the fourth being almost parallel to the surface. The light and dark regions are due to the contrast provided by twin formation in a single variant. The field of view is about 1mm.

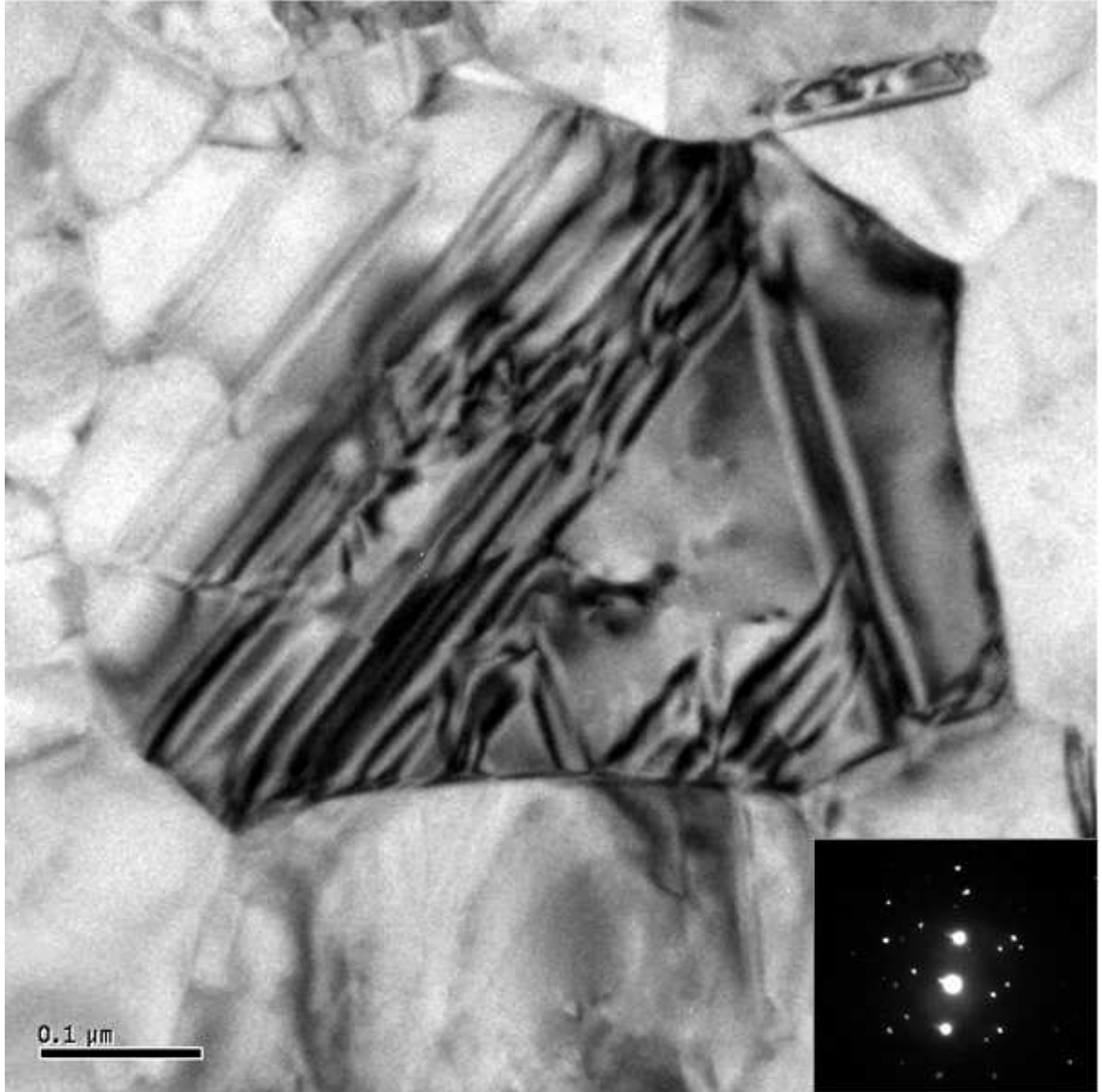


Figure 4.2: *TEM image of a 50 nm thick Co-Ni 50 film. The film was annealed at 650 °C for 6 hours. The description of the morphology follows from figure 4.1. The diffraction pattern clearly shows the twinned nature of the grain by the secondary spots*

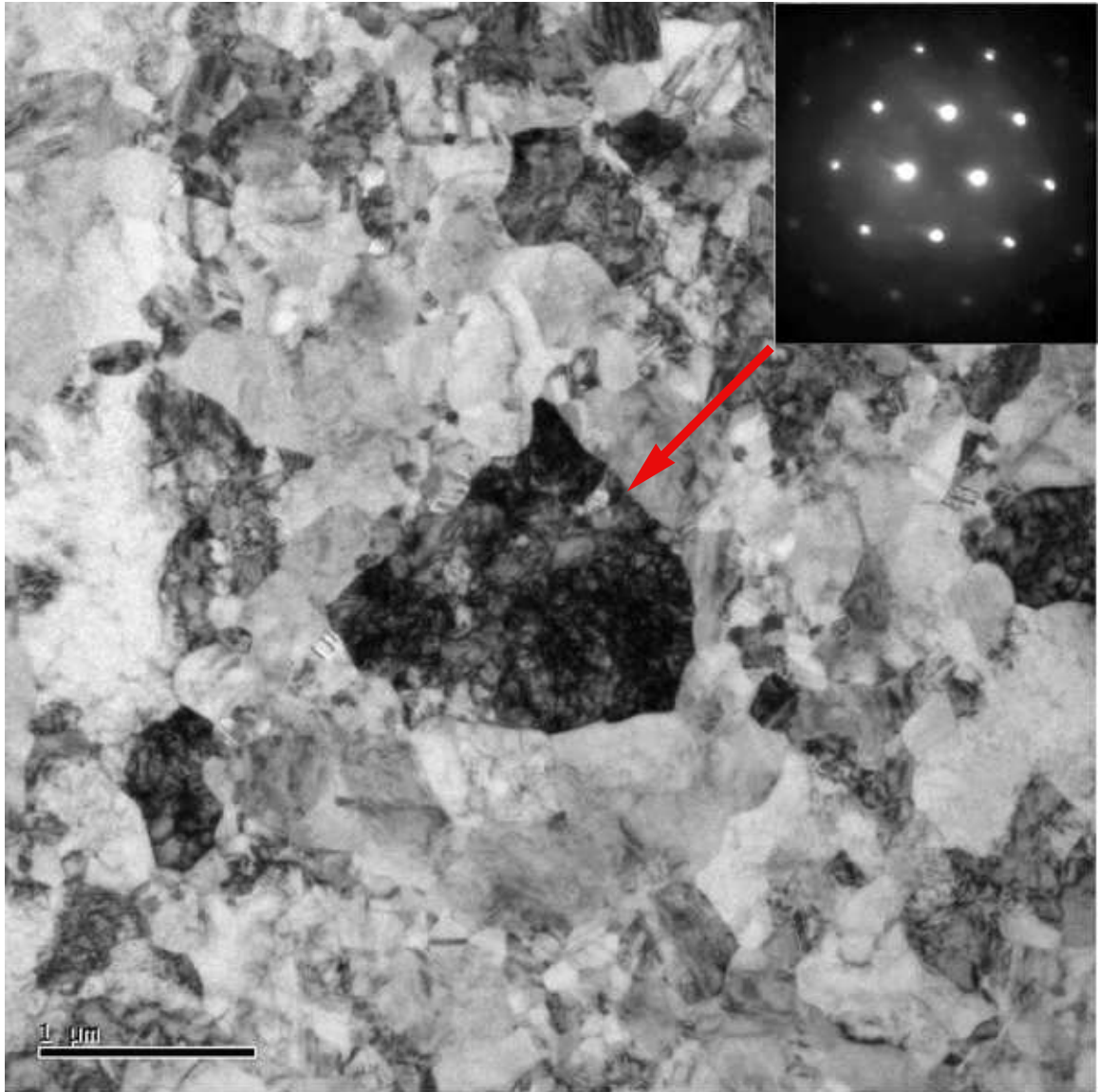


Figure 4.3: *TEM image of a 50 nm thick Co-Ni film. The large grain at center is a fcc phase (as seen from the dp) and is significantly bigger than the film thickness. However, the average grain sized is about 100 nm.*

thickness.

Composition measurement techniques such as secondary ion mass spectrometry (SIMS) are not feasible because the similarity in mass of cobalt and nickel.

4.2 structural analysis

Both microscopy and x-ray diffraction were used to examine structure. TEM will be discussed more in chapter 5, but one important result was that films were found to be of mixed phase. Some grains were hexagonal and other grains were cubic.

X-ray diffraction was the major analytical tool and was used mainly to determine phase and texture of the films. Because the 111_{fcc} peak is very close to the 0002_{hcp} , the relative height of the 200_{fcc} peak, as well as the strength of the 101_{hcp} peak was used to determine qualitatively which phases were present.

In theory, the close-packed peaks for hexagonal and cubic phase Co-Ni alloys should be distinguishable. However, experimentally, these alloys have so many stacking faults (due to martensitic transformation) that the peaks overlap and are difficult to deconvolve. Taylor [41] discusses the difficulty in distinguishing between the cubic and hexagonal phases, and provides extensive bulk analysis. In the case of the 15% alloy, it was possible to deconvolve the film peak into two distinct peaks corresponding correctly in position and intensity to the hexagonal and cubic phases (see figure 4.5).

As a reference, the peaks for fcc and hcp cobalt as well as fcc nickel were compiled from powder diffraction files and are presented in table 4.2

Figure 4.4 shows a comparison of 10%, 15%, 20%, and 30% thin-film samples. Of interest is the disappearance of the 200_{fcc} peak as the weight percent of nickel decreases. Conversely, the 101_{hcp} becomes more prominent until 15 wt%Ni, and is gone for 10

| peak | 2θ | intensity | $d_{hkl}(\text{\AA})$ |
|-------------------|-----------|-----------|-----------------------|
| <i>fcc cobalt</i> | | | |
| 111 | 44.215 | 100 | 2.0460 |
| 200 | 51.512 | 40 | 1.7720 |
| 220 | 75.821 | 25 | 1.2532 |
| 311 | 92.720 | 30 | 1.0680 |
| 222 | 97.648 | 12 | 1.0230 |
| <i>hcp cobalt</i> | | | |
| 100 | 41.668 | 20 | 2.1650 |
| 002 | 44.745 | 60 | 2.0230 |
| 101 | 47.549 | 100 | 1.910 |
| 102 | 62.701 | 1 | 1.4680 |
| 110 | 75.906 | 80 | 1.2520 |
| 103 | 84.157 | 80 | 1.1490 |
| 200 | 90.631 | 20 | 1.0830 |
| 112 | 92.494 | 80 | 1.0660 |
| 201 | 94.688 | 60 | 1.0470 |
| <i>fcc nickel</i> | | | |
| 111 | 44.490 | 100 | 2.0340 |
| 200 | 51.826 | 42 | 1.7620 |
| 220 | 76.337 | 21 | 1.2460 |
| 311 | 92.900 | 20 | 1.0172 |
| 222 | 98.397 | 7 | 0.8810 |

Table 4.2: *Diffraction pattern standards for nickel and cobalt. Of interest is the similarity between fcc cobalt and fcc nickel. Also, note that the 111_{cubic} and 002_{hex} peaks are very close.*

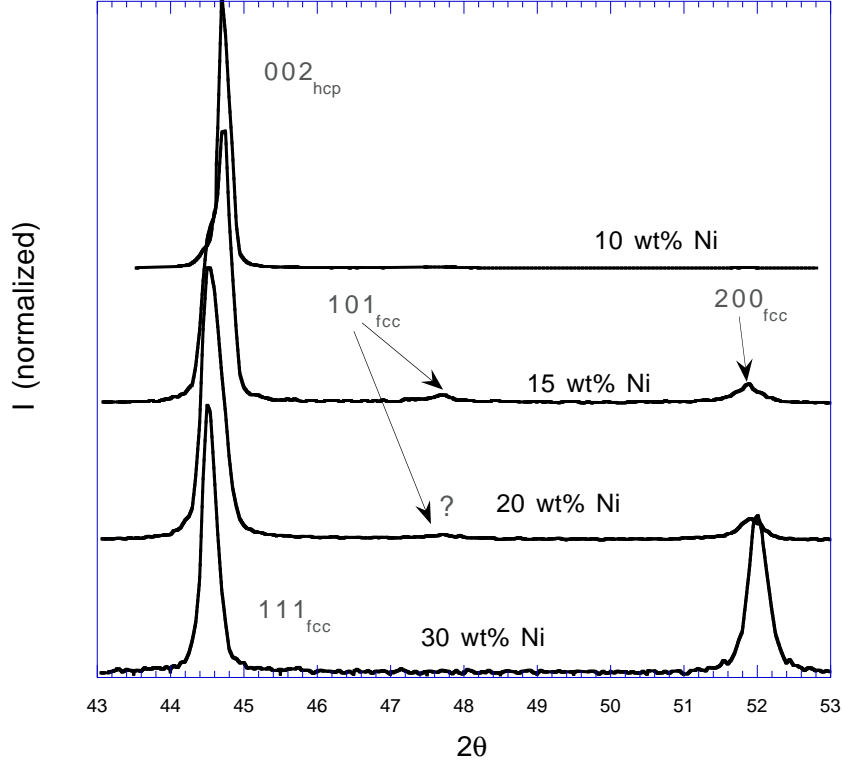


Figure 4.4: *X-ray diffraction patterns of four different compositions of thin-film Co-Ni alloys . The film peak changes from 111_{fcc} to 002_{hcp} .*

wt%Ni. Also of interest is that the trend of the 111_{fcc} (002_{hcp}) peak toward higher values of 2θ has nickel content decreases. Even though the diffractometer is not accurate enough in 2θ to get absolute d-spacing, the relative change in spacing can be extrapolated from the data. This information is useful in calculating the transformation matrices from chapter 3. Taylor [41] shows that an accurate way to determine phase transformation in Co-Ni alloys is by the distance between the 111_{fcc} peak and the 200_{fcc} peak. Clearly in figure 4.4 as the nickel content decreases these peaks move closer together. So while the 200_{fcc} peak does not change in relative intensity between 20% and 15%, the two peaks do move closer together.

Figure 4.6 show a 25wt%Ni bulk alloy. Of interest is the idea that stress, from polishing in this case, can have the same effect as decreasing the nickel content. In other words the ratio of the intensity of the hexagonal to cubic peaks decreases after

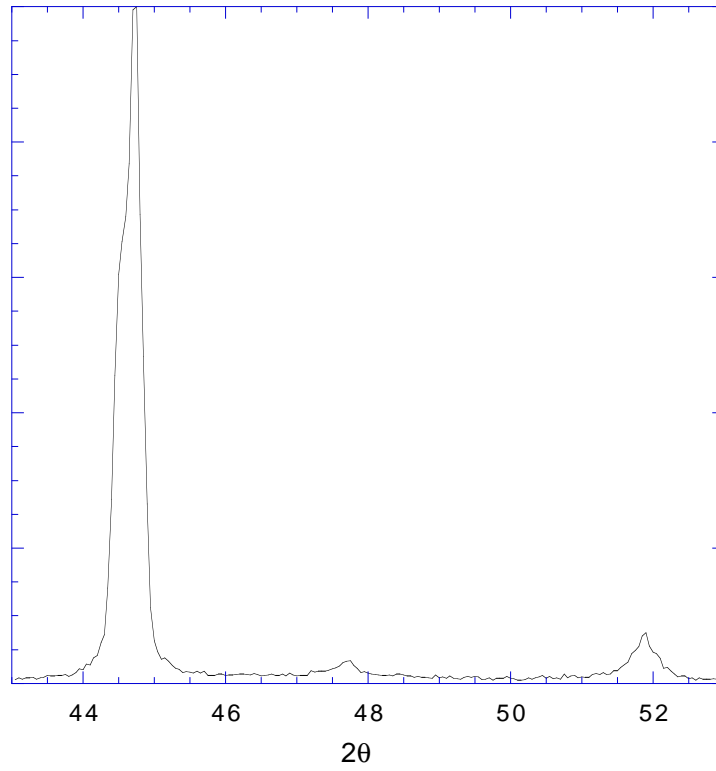


Figure 4.5: *Log plot of xrd data for 15% film. Note that both the hcp and fcc close packed peaks are distinguishable, indicating a comparable amount of fcc and hcp grains. Also, note the presence of both the 200_{fcc} and 101_{hcp} peaks. Refer to figure 4.4 for peak positions.*

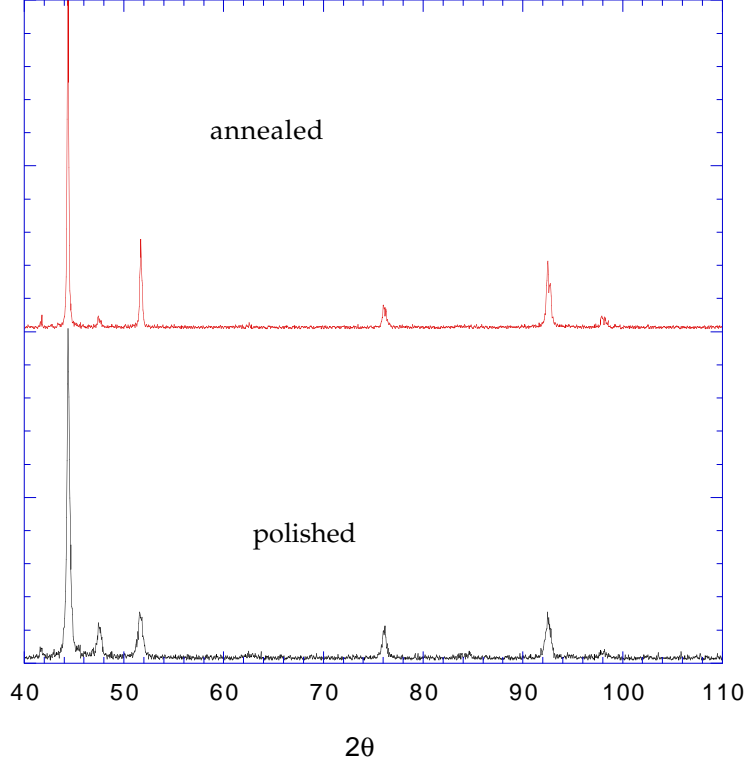


Figure 4.6: *Bulk 25wt%Ni bulk alloy. Annealed in vacuum at 300°C for 12 hours. Refer to table 4.2 for diffraction peak information*

the sample has been annealed.

Figure 4.7 show the peak positions for a bulk sample as compared to a thin-film sample (500 nm). What is of interest is that the peak separation in the thin-film is much greater than the bulk annealed or unannealed sample. In order to correct for the diffractometer error in 2θ , the data has been normalized in 2θ to show the peak shift. The data can be interpreted qualitatively in one or more of the following ways:

1. The 200_{fcc} spacing has decreased (due to a compressive stress).
2. The 111_{fcc} (002_{hcp}) spacing has increased (tensile stress).
3. The relative amount of the hexagonal phase has decreased due to film stress, thus shifting the 111_{fcc} (002_{hcp}) peak lower in 2θ .

The last item is of particular interest because it would indicate that the martensitic transformation has been retarded in the thin-film.

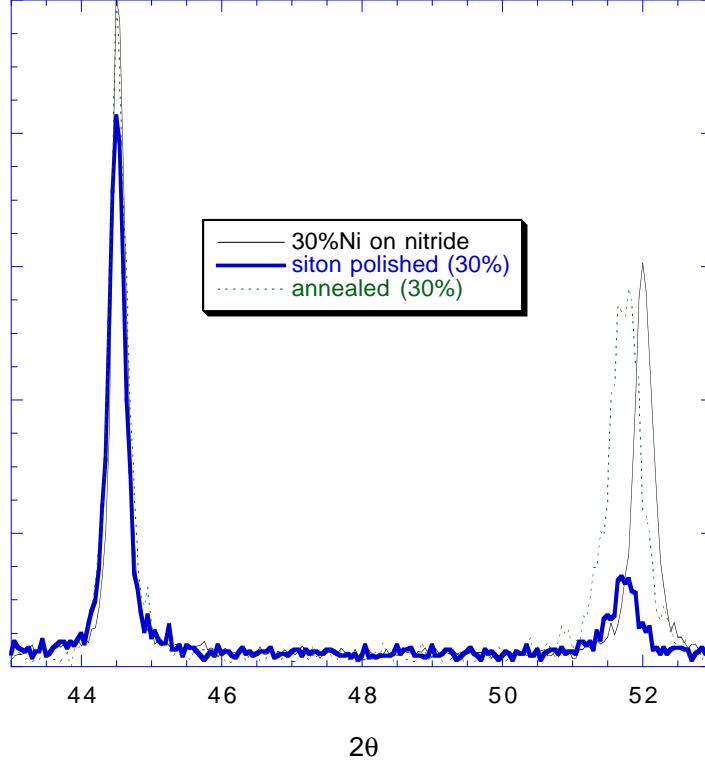


Figure 4.7: *30wt%Ni bulk and thin-film samples.*

One last interesting note is the comparison of films grown on nitride with films grown on oxide. Figure 4.8 shows two 500 nm films. What is of interest is that the relative intensity of the $(111)_{\text{fcc}}$ ($(002)_{\text{hcp}}$) peak to the $(200)_{\text{fcc}}$ peak should be about 2:1 *for a perfect powder sample*— that is one in which all grains are represented equally with respect to the x-ray beam. In figure 4.8 one can see the film grown on oxide represents expected texture for metal films grown on amorphous substrates— the $(111)_{\text{fcc}}$ ($(002)_{\text{hcp}}$) planes lie parallel to the substrate—indicating a very strong texture by the relative weakness of the $(200)_{\text{fcc}}$ peak.

However, the film grown on a nitride substrate³ shows a large relative intensity of the $(200)_{\text{fcc}}$ peak. This can only mean the film has developed a strong 'cubic' texture. This phenomenon is very unusual. One possible explanation is that the metal film did not adhere well to the nitride and martensitic transformation caused the orientation

³this has been duplicated in three different films

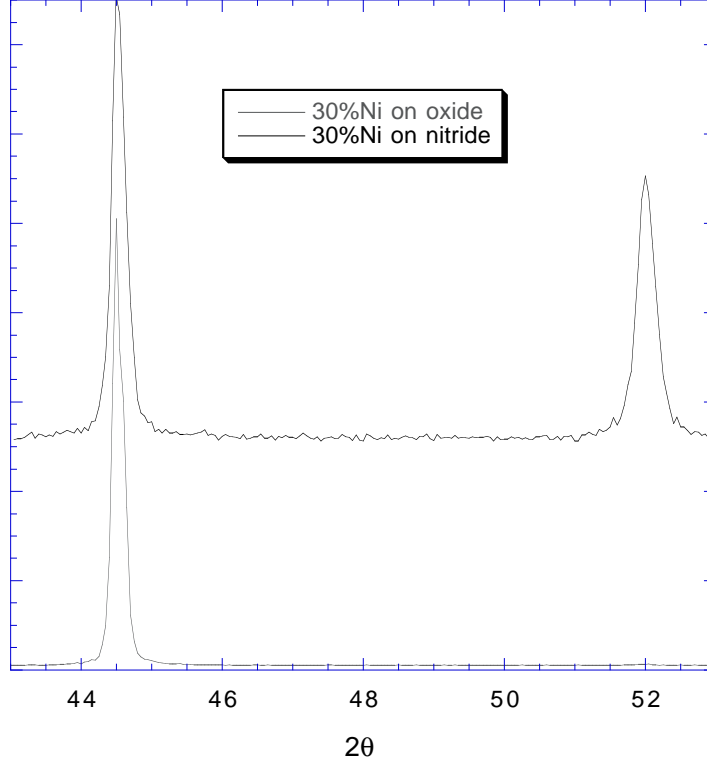


Figure 4.8: *30wt%Ni film grown on oxide and nitride substrates.*

of the grain to shift from the preferred close-packed texture.

4.3 magnetic measurements

The main purpose of magnetic measurements on the samples was to establish the polarization data. Of primary interest is the saturation magnetization, M_s and the technical saturation value of magnetic field, H_s . which can both be obtained from a hysteresis loop. H_s as well as the shape of the hysteresis curve can give phase information while M_s is important in determining the magnetocrystalline and shape anisotropy.

All measurements were done on a Quantum Designs SQUID magnetometer which can apply fields of up to 5T, using a superconducting magnet, and has sensitivity down to 10^{-6} emu/cm⁻³. In this section only in-plane measurements of magnetization will

be presented.

One would expect M_s to decrease with increasing nickel content because nickel has a much lower value of M_s in any crystallographic direction, 480 kA/m for nickel, and 1300 kA/m for cobalt when measured in the close-packed direction [24]. Also, one would expect H_s to increase for decreasing nickel content because the in-plane direction is changing from a relatively easy $\langle 112 \rangle$ texture to a basal (hcp) texture). For example, H_s in nickel is 1000 A/m (in the $\langle 112 \rangle$ direction) and in the $\langle 110 \rangle$ direction in cobalt H_s is 80 kA/m.

These concepts are illustrated in figures 4.9, 4.10 4.11. The values of H_s found for 10, 15, 20, and 30wt%Ni are 96, 80, 64, and 7 kA/m respectively. Interestingly enough, the value of the applied field necessary to saturate the sample (H_s) was an excellent indicator of what the majority phase of the film was. The switch from a mostly cubic phase to a mostly hexagonal phase film occurs between 30 wt% and 20 wt% Ni. Thus, a dramatic increase occurs in H_s from about 560 A/m for 30 wt% to 4720 A/m for a 20 wt% film; but only a small increase occurs between 20 wt% and 10 wt% Ni. This is explained by the fact that a cubic film has a relatively easy axis of magnetization in-plane, whereas the hexagonal film has a hard axis in-plane, as discussed previously.

4.4 magnetostrictive measurements

The measurement of magnetostriction on thin-films presents many unique problems. Some problems are resolved by using standard techniques for measuring stress in thin-films. These techniques include capacitive, acoustic, and elipsometry (and other forms of interferometry) methods. An excellent review is presented by [42].

In order to determine the most accurate and efficient method for magnetostriction the parameters of the system have to be reiterated. The films are typically on the order

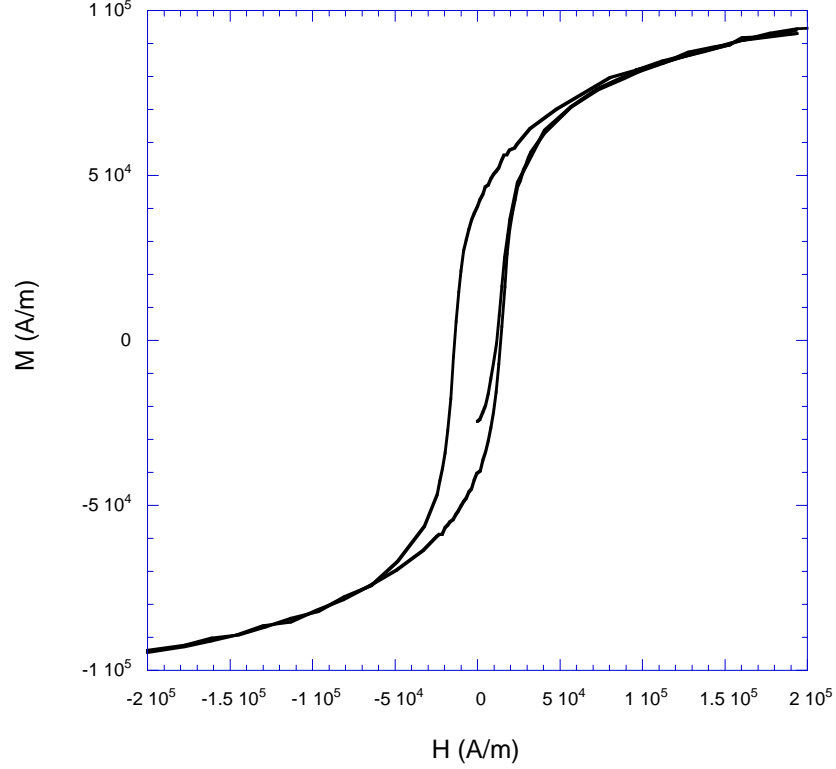


Figure 4.9: *Hysteresis data for a 400 nm Co: 15wt%Ni film grown on nitride (300K).*

of 500 nm, the polarization field is less than 1 T, and the minimum magnetoelastic strain (at saturation) is about 10^{-5} .

For these conditions it was decided to use a cantilever deflection measurement system with a standard electromagnet.

4.4.1 cantilever deflection

The theory for the deflection of a cantilever due to strain in a coherent film is well established [43, 44]. For the geometry shown in figure 4.12 with the length:width:thickness ratio being 100:10:1, Nix⁴ derives the following equation for the end displacement [45]

$$d = \frac{\lambda L^2}{h_s} \quad (4.2)$$

⁴the key here is that the film is no more than 1% the thickness of the substrate

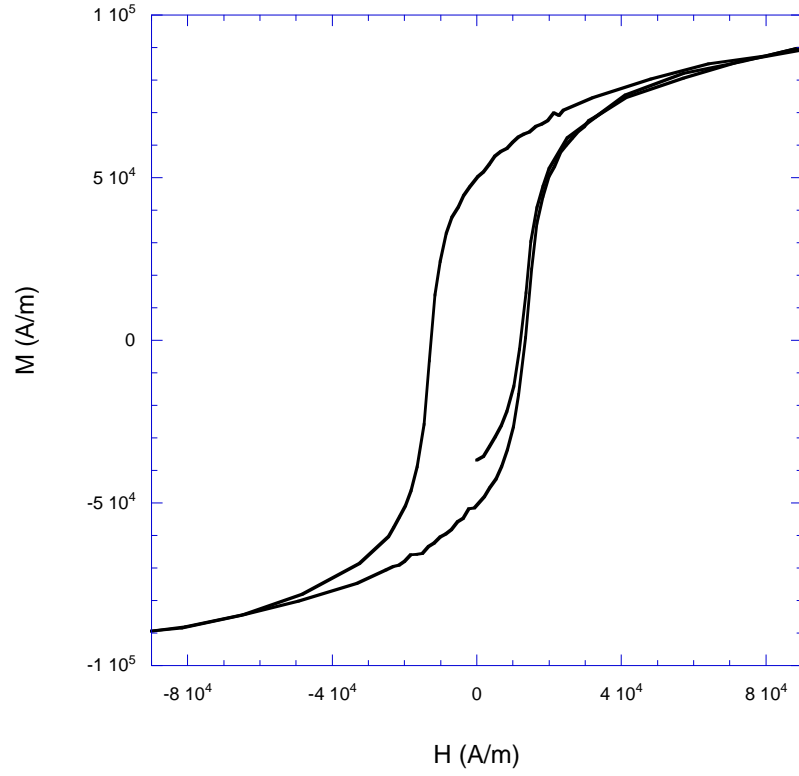


Figure 4.10: *Hysteresis measurement of a 500 nm Co: 20wt%Ni film grown on nitride (300K). Note that the remnant field is higher than the 15wt% sample. Also, the saturation field is lower as is M_s .*

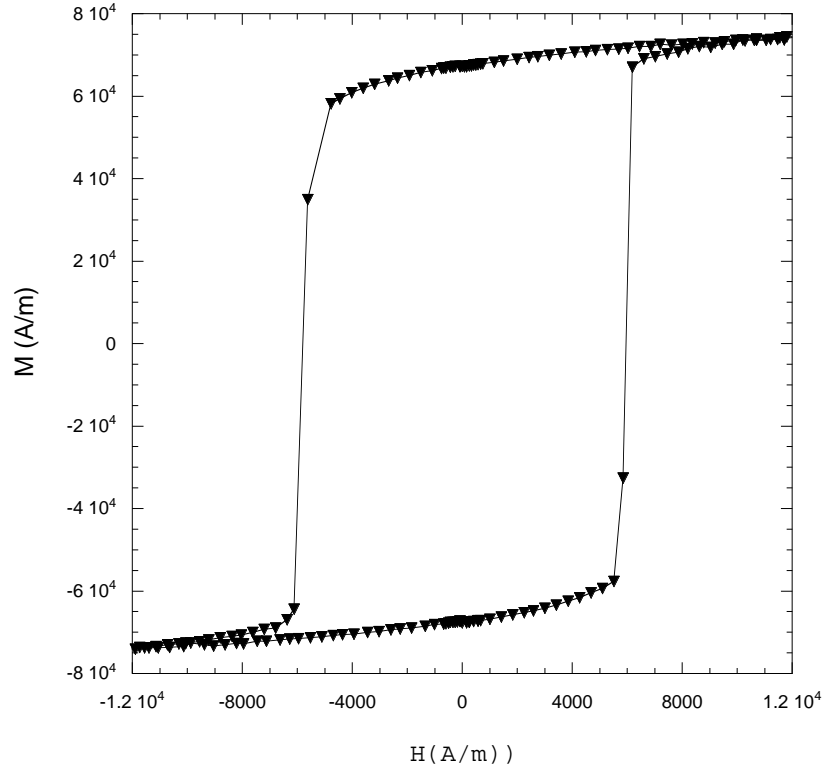


Figure 4.11: *Hysteresis measurement of a 200 nm Co: 30wt%Ni film grown on nitride (300K). Note that the hysteresis loop for this sample is quite square, in contrast to the 15 wt% and 20 wt% Ni sample. Data points are included to show high remnant field.*

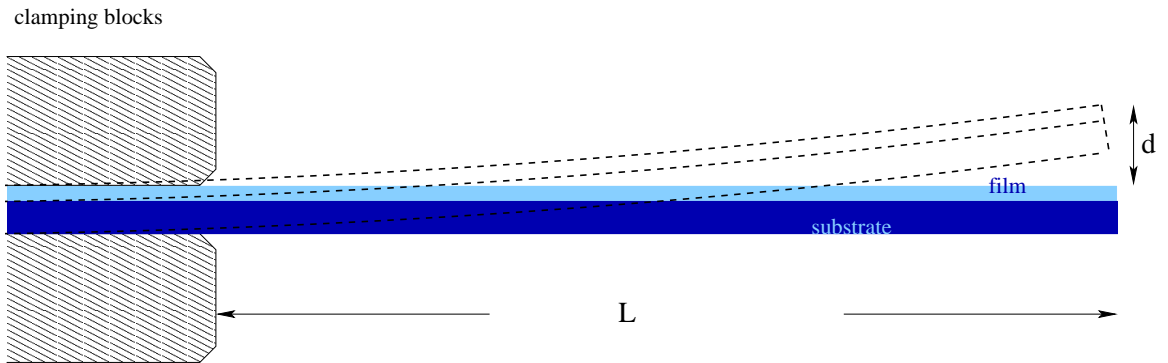


Figure 4.12: *Cantilever deflection setup. The cantilever is fixed at one end. Upon magnetization the deflection (shown as the dashed line) due to the contraction of the film can be measured.*

or for the case where strain is of interest

$$\lambda = \frac{h_s d}{L^2}. \quad (4.3)$$

This is a very elegant solution because it is independent of the material properties and gives the strain in the film as a function of three easily measurable parameters, L , d , and h_f . The cantilevers are fabricated by dicing up the substrates and then chemomechanically polishing the substrates down to a thickness which can be handled safely but is still thin enough to provide good deflection data. For example, the substrates are polished from 500 μm to 50 μm using siton and hydrogen peroxide.

At this point it is instructive to estimate what the end deflection of a cantilever would be assuming a strain of 10^{-5} . Using a cantilever 25 mm long by 50 μm thick gives an end displacement of 208 μm . This displacement can actually be seen by the human eye.

With a displacement on the order of hundreds of μm , one can use an optics system to measure. Figure 4.13 shows a schematic of the measurement setup. A long range microscope is used to narrow the field of view down to 1 mm. A digital camera using a pixel detector with pixel dimensions of 800x1200 gives a resolution of about 1 pixel per μm of deflection. The 2X eyepiece includes a reticle which is used to measure the deflection. The reticle can be calibrated by accurately measuring the thickness of the cantilever. Figure 4.14 shows an image of a cantilever taken with the setup.

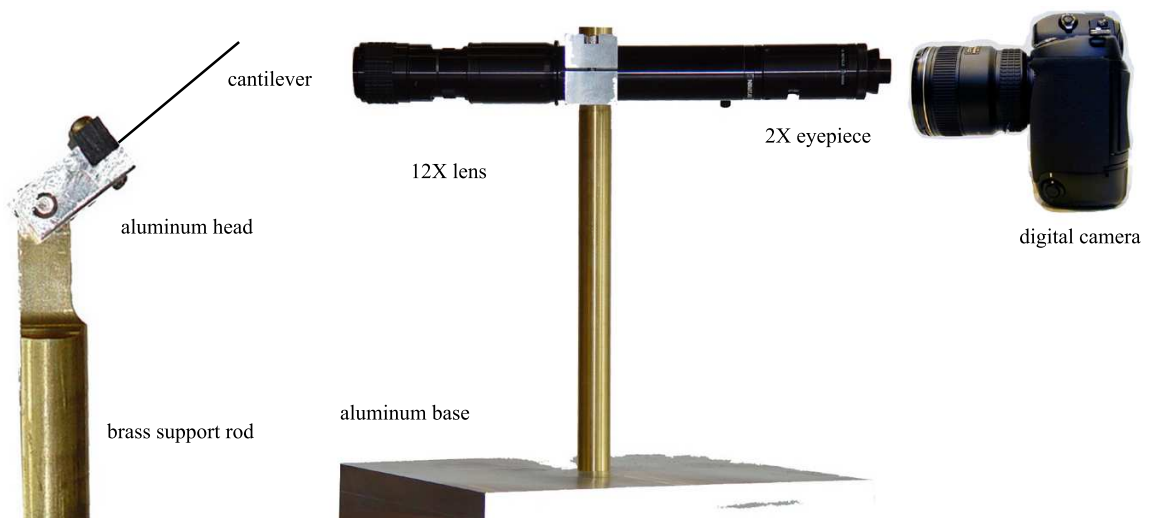


Figure 4.13: *Cantilever deflection measurement setup for magnetostriction measurements. All components are 'non-magnetic' (brass, stainless steel, delrin, and aluminum). Components are not to scale.*

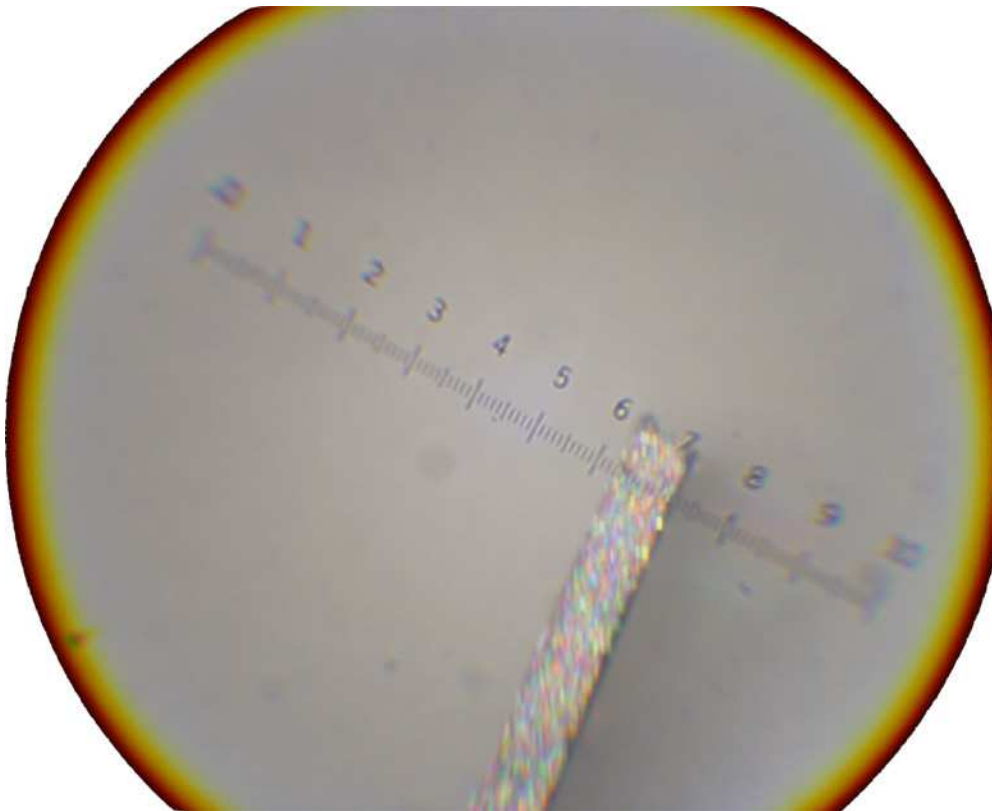


Figure 4.14: *Digital image of a silicon cantilever in the magnetostriction measurement apparatus. The cantilever is 0.1 mm thick.*

Chapter 5

Results and Conclusions

Although giant magnetostriction was the hoped for result, it was not found. However there were other important results that came out this study. This chapter will include a brief discussion of the cantilever measurements. More discussion will be given to observations of microstructure and of a novel magnetoelastic measurement technique.

5.1 cantilever deflection measurement of magnetostriction

The cantilever deflection apparatus has been described previously in chapter four, in addition to that information it is also useful to know what the magnetic environment was. The measurements were conducted using a Bruker electromagnet (non-superconducting). The maximum field was 1.2 T and the field was uniform to within 10^{-4} T over a cylindrical volume of 50 mm diameter by 100 mm in length, which was more than sufficient to provide uniform field conditions for the cantilevers.

The cantilever holder has two axes of rotation and the height could be adjusted, thereby assuring a uniform field for any orientation of the film relative to the magnetic field.

5.1.1 experimental results

Cantilevers of all compositions were made and measured. The field was varied from .005 T to 1.2 T in increments as small as .002 T and as large as 0.1 T. There was a small deflection seen at lower fields but no significant deflection was seen until fields which were many times higher than what was measured to saturate the films (in the in-plane case).

One of the issues with the measurement technique was in ensuring that the film was subject to a uniform orientation to the field. If the film is not uniformly oriented to the field, the cantilever can experience a torque due to magnetic field. Since the cantilevers were slightly curved because of intrinsic stress (due to mismatch in coefficient of thermal expansion) the uniform condition was never met. Figure 5.1 illustrates this concept.

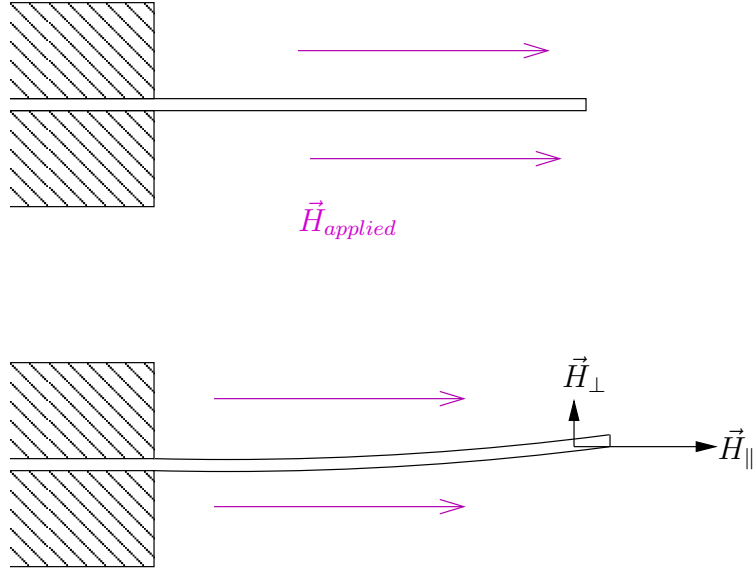


Figure 5.1: *At top, a parallel cantilever experiences no dipole torque due to the applied field. When the cantilever is no longer parallel, a resolved perpendicular component of the field leads to a variable load on the the cantilever (due to the dipole torque) which causes an end deflection of the cantilever (due to the end constraint).*

Figure 5.2 shows a typical result for a Co: 20 wt% Ni film. This data is for a 500 nm thick film on nitride. The cantilever is 0.1 mm thick and 25 mm long.

From magnetic measurements, the saturation value of magnetization for this film is about 200 kA/m. To ensure the film went from a demagnetized state to a saturated state, the cantilever was magnetized along its length (in-plane) and then the field was reversed (or the cantilever rotated by 180 degrees).

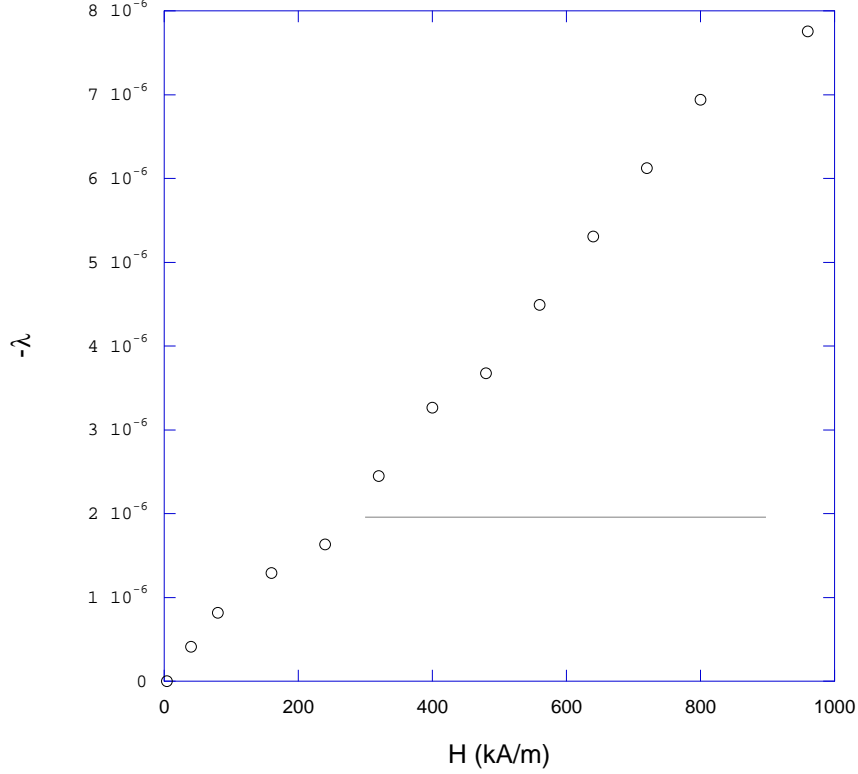


Figure 5.2: *Magnetostriction measurement of a 25 mm long by 0.1 mm thick cantilever. The sign of the strain is negative because the cantilever was concave with the films side in, meaning the strain was tensile. The dashed line shows the asymptotic value of λ_s^{ip} .*

It is difficult to determine the exact contribution of a magnetic torque due to non-parallel orientation of the cantilever, but I estimated this strain to be much less than the magnetostriction (for fields less than 0.5 T). It is a good estimate to take the value of strain at the saturating field as the magnetostrictive constant for the in-plane configuration. Examining figure 5.2 yields a value of $\lambda_s^{in-plane}$ of about -2×10^{-6} occurring at about 200 kA/m. This value is within reason, given the estimates in chapter three, but clearly can be attributed to strictly magnetoelastic origins. In

upcoming sections these values will be independently verified.

The data for the other compositions and film thicknesses gave comparable values of in-plane magnetoelastic constants, with values for $\lambda_s^{in-plane}$ ranging from -10^{-6} to -10^{-5} . All magnetostriction observed was negative in sign meaning a tensile strain.

5.2 microstructure and film morphology

The microstructure observed in the films was discussed in, but it bears more analysis. Figures 5.3, 5.4, and 5.5 show field emission scanning electron micrographs of different composition films on different substrates with different annealing conditions.

Figure 5.3 shows a 500 nm thick film grown on silicon nitride and annealed at 600 °C . Compare this to figure 5.4, which is a 200 nm film annealed at 450 °C . The 500 nm film annealed at higher temperature clearly shows a highly textured film, which is to say the grains are wide and parallel to the substrate. The thinner film annealed at lower temperature shows equiaxial grains of fairly uniform size. While

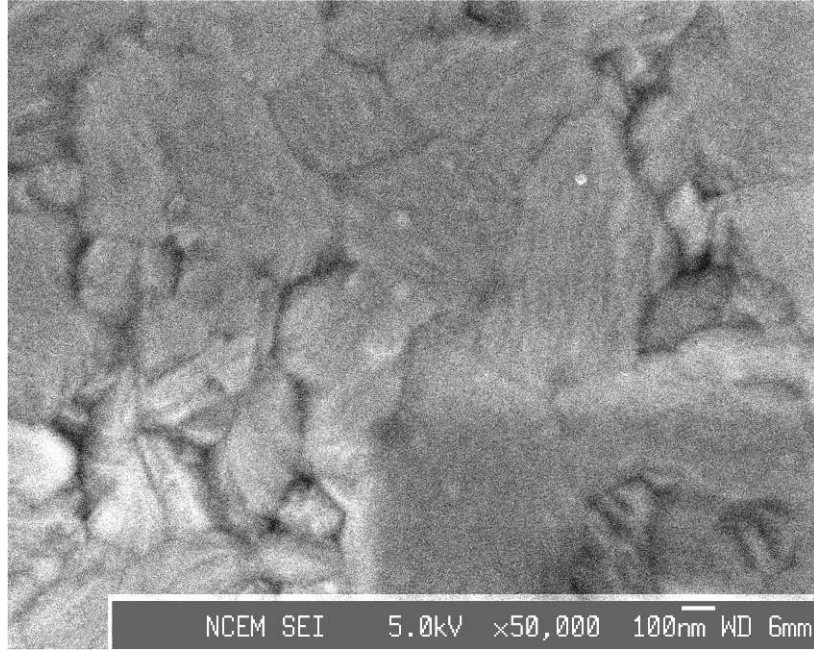


Figure 5.3: 500 nm 20 wt% Ni film annealed at 600 °C .

both films show a hexagonal character, the grains in figure 5.4 illustrate the transformation process by the parallel bands visible on many grains. In the case of the uniaxial grains, the grains are still textured $\{002\}_{\text{hcp}}$ with respect to the substrate, however they are free to transform on more one close packed plane (as discussed in chapter three). In the case of the film annealed at a higher temperature, which x-ray diffraction indicates is also transformed, the flat plate-like morphology would seem to indicate that the transformation takes place almost entirely on planes parallel to the substrate.

I believe the difference in morphology is due to annealing conditions, either by raising the homologous temperature giving rise to a different zone (growth mode), or by providing better adhesion to the substrate. The film thickness probably does not play a critical role in determining the morphology and microstructure. As evidence

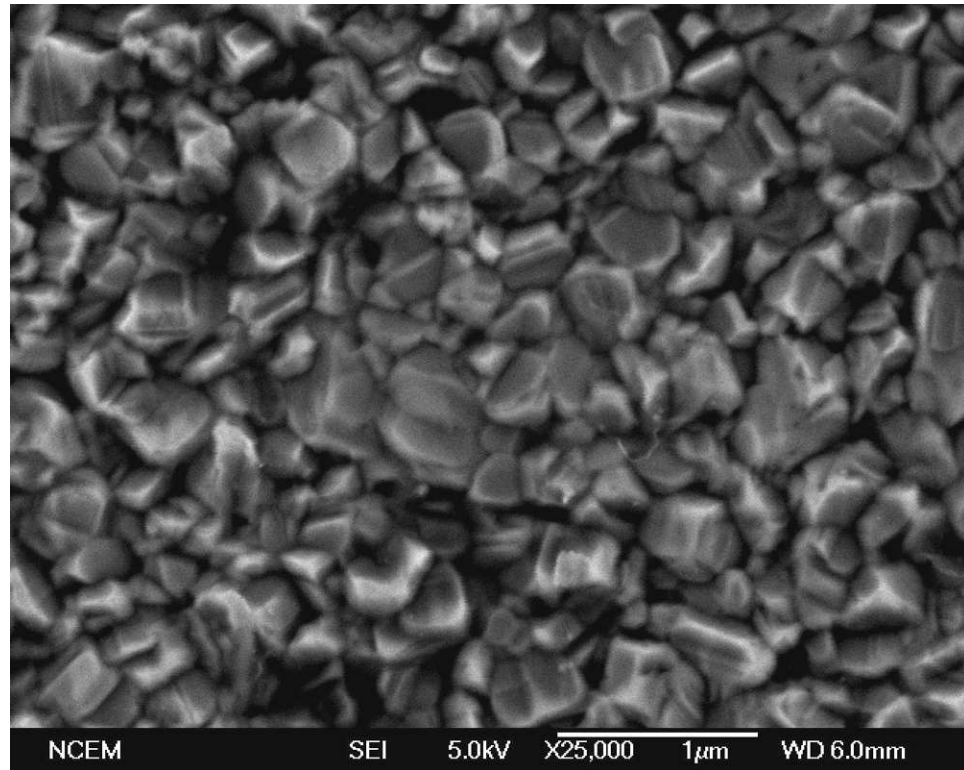


Figure 5.4: *200 nm 20 wt% Ni film annealed at 450 °C . Not that the grains are equiaxed and of relatively uniform size. The bands across the grains are transformation (or slip) planes.*

of this consider figure 5.5 which is a 50 nm thick film on oxide, annealed at 650 °C . The grain size and shape are similar to the TEM images of the 50 nm film grown in nitride in chapter four. It is interesting to note in these films is the fact that a very thin, constrained film can still display the full range of bulk-like morphology. Two interesting features are the grain with the parallel transformation bands (upper left) and the large region of defected grains at top center, which is similar to optical micrograph in chapter four.

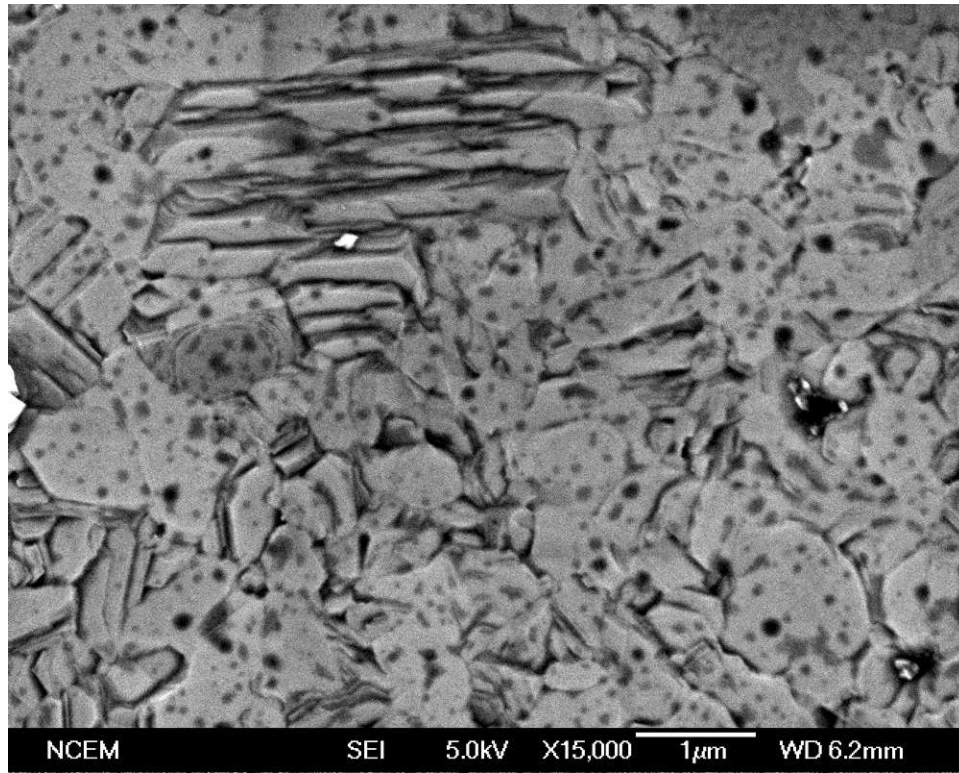


Figure 5.5: 50 nm 30 wt% Ni film annealed at 650 °C . Note the large grain size and textured morphology. At the upper left is a grain with two parallel transformation bands. At top center is a distorted region, showing a similar morphology to bulk samples.

5.3 a novel magnetoelastic characterization technique

The cantilever measurement system is fairly straightforward in terms of relating deflection to strain, but the experimental procedure proved to be quite difficult. Although the values obtained with the cantilever deflection setup are reasonable, it is useful to have an additional method to corroborate the results.

Because the magnetic properties of Co-Ni alloys change when there is a phase transformation [22]; one can measure the magnetization of a sample as it is being cooled or strained and use this information to determine phase transformation parameters.

Early on in this research the in-plane magnetization was measured as a function of temperature to see such an effect. Although no clear evidence of phase transformation was seen, I noticed that the dependence of magnetization on temperature varied in a predictable manner. I hypothesized that this variation in magnetization was magnetoelastic in nature, and I began to search for a model to explain this effect.

The hypothesis I settled on was that a temperature dependent stress was present due to the mismatch in the coefficient of thermal expansion (CTE) between the substrate and film. Thus the key was to be able to relate the difference in CTE to a stress, and then relate the stress to the magnetization.

The well known Stoner-Wohlfarth [25] model gives a relation between stress and magnetization for a uniaxial material. A film can be treated as a uniaxial system if the normal direction to the film is a hard axis and the in-plane direction is an isotropic easy axis (or 'easy plane'). This condition can be met when the magnetocrystalline anisotropy energy (in-plane) is less than the anisotropy energy due to magnetostatics (also called 'shape anisotropy').

5.3.1 Application of the S-W model to Co-Ni thin films

For a $\{111\}$ textured cubic film, the $\langle 111 \rangle$ direction (out of plane) is an easy axis and has low anisotropy energy. For $\langle 112 \rangle$ type directions, the anisotropy is higher. The difference between these two terms must be less than the shape anisotropy for a thin film, $\frac{\mu_0 M_s^2}{2}$. For Ni, this value, $|u_a^{\langle 111 \rangle}| - |u_a^{\langle 112 \rangle}|$, is about 10^3 J/m^3 .

For the hexagonal textured thin films the easy magnetocrystalline axis is also perpendicular to the film plane. However, cobalt has an magnetocrystalline anisotropy energy of about $5 \times 10^5 \text{ J/m}^3$. Since the measured saturation value of magnetization for the alloys is around 10^5 A/m , then the shape anisotropy energy is about 10^5 J/m^3 for the films. Thus, the magnetocrystalline anisotropy of any of the alloy films is less than the value for pure cobalt if the easy axis of magnetization is in-plane. This is supported by the magnetization curves in chapter four, although as the amount of nickel increases the magnetization curves become less and less square. In fact, the 10 wt% Ni film has a saturation value of almost 100 kA/m which is a significant fraction of H_a . This shows that the magnetocrystalline anisotropy energy is moving closer to the value for pure cobalt.

If the hexagonal films and the highly textured cubic films can be treated as uniaxial, the Stoner-Wolfarth model can be applied as a good approximation. Figure 5.6 illustrates the fundamental ideas of this problem. Essentially, one measures the in-plane magnetization as a function of temperature. This data is then compared to a theoretical model which is based on the Stoner-Wolfarth problem, and the saturation value of magnetostriction is used as a fitting parameter.

Appendix B gives a complete derivation of the in-plane magnetic moment as a function of applied stress. The result is (in MKS units),

$$M = M_S \sqrt{1 - \left(\frac{\mu_0 M_s^2}{6\lambda_s \sigma + 2\mu_0 M_s H_a} \right)^2} \quad (5.1)$$

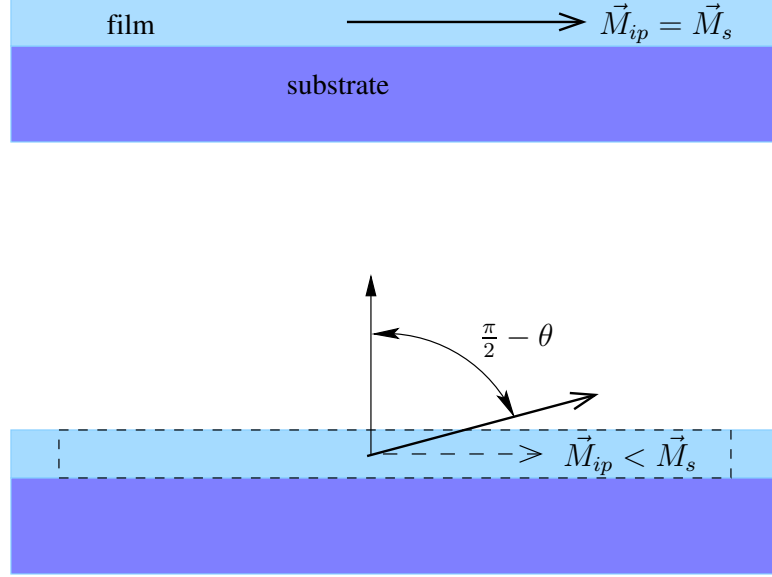


Figure 5.6: *At top, the film is relaxed and the in-plane magnetic moment is equal to the saturation value of magnetization. At bottom, the film has been cooled and, because the film is constrained by the substrate (the dashed rectangle shows what shape the relaxed film would be), it experiences an effective positive tensile strain. This imposed strain causes the magnetic moment to lie more and more out of plane (for a negative λ_s) as strain is increased. This results in the measured in-plane magnetization decreasing.*

where H_a is the field necessary to saturate the sample in the hard direction (perpendicular to the film). The stress, σ , can be replaced by E , the elastic modulus, times the imposed strain ε_i which is calculated from the mismatch in coefficient of thermal expansion.

Although there is an intrinsic stress of about 10 MPa at room temperature, this stress does not need to be included in the fit because we are only concerned with *changes* in the stress (strain) state of the thin film.

5.3.2 Strain due to CTE mismatch

The value of strain due to CTE mismatch was tabulated as follows. First the difference in the CTE for silicon, and nickel (or cobalt)¹ with temperature was measured (figure 5.7). The curve was numerically integrated to obtain a cumulative strain as a

¹cobalt and nickel have almost identical values of α

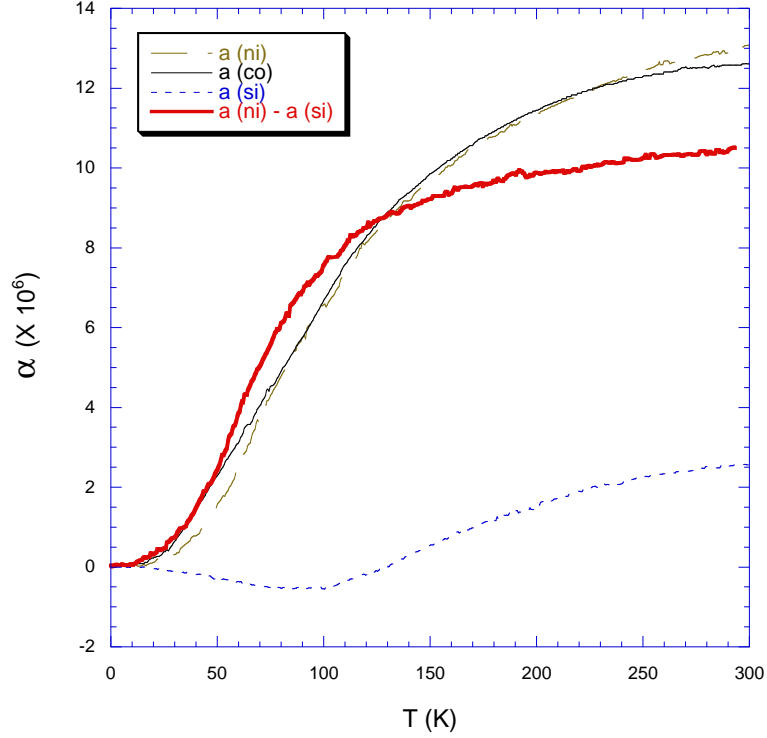


Figure 5.7: Coefficient of thermal expansion for Si, Co, and Ni as a function of temperature. Data taken from [46].

function of temperature (figure 5.8). This strain is such that it increases for decreasing temperature (as one would expect). The cumulative strain data is then fed into 5.1 and that curve is fitted to M-T data taken with the SQUID by adjusting the value of λ_s . Although it is probably more accurate to use a combination of CTE data for SiO₂ and silicon in calculations. However it makes very little difference because the CTE for silicon is small and fairly constant and the variation of α with temperature between 300 K and 0 K is essentially zero for SiO₂. Also, note that the values for the CTE of cobalt and nickel are very close in the temperature range of interest, thus it is probably accurate to take the value of α_{Ni} or α_{Co} for any of the alloys.

Two important facts about figure 5.7 and figure 5.8 should be mentioned. First, the CTE data are asymptotic for T greater than 350 K. This means the model should be give a concave-down curvature for larger values of λ_s . Also, the CTE data are asymptotic toward 0 K. Secondly, the cumulative strain has a pronounced knee at

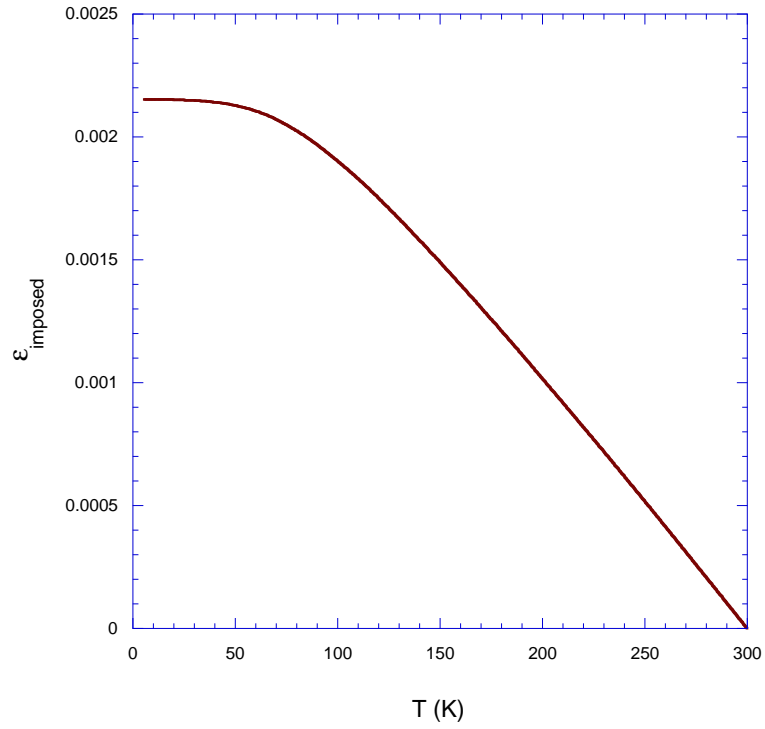


Figure 5.8: *The cumulative strain experienced by the film due to the difference in CTE. The strain increases with decreasing temperature and is derived by numerically integrating the $\alpha_{Ni,Co}(T) - \alpha_{Si}(T)$.*

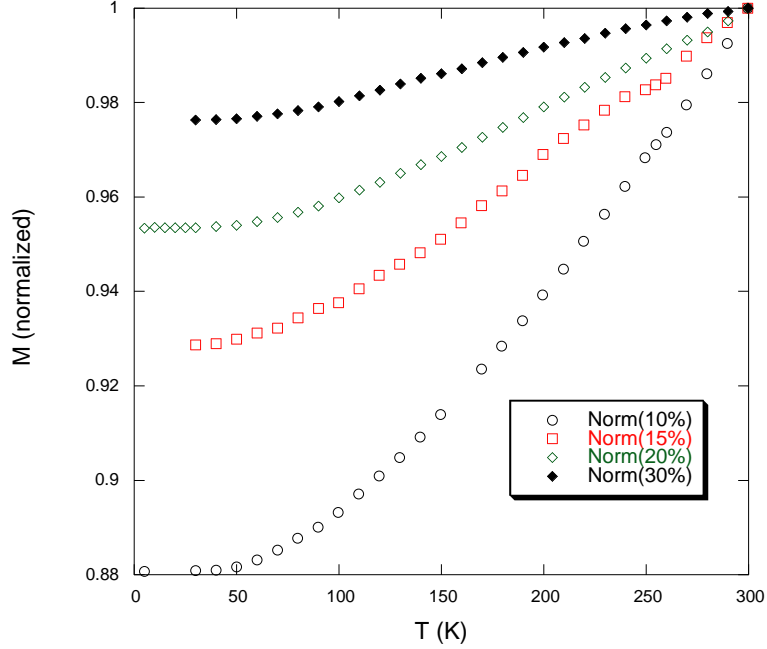


Figure 5.9: *In plane magnetization as a function of temperature for four different composition films. The value of M_{ip} is normalized to enhance the difference between different compositions.*

about 100 K and that should appear in all plots, as long as the value of α does not stray from that of cobalt or nickel.

5.3.3 Results of uniaxial model

Equation 5.1 was fitted to films grown from all four alloy compositions. The model was very accurate and small changes in anisotropy energy and magnetostriction changed the fit to accommodate significant differences in data for different alloys.

Figure 5.9 shows the magnetization of four thin films as a function of temperature between 0 and 300 K. The percent difference in M_{ip} (the in-plane moment) increases with increasing cobalt concentration. The films were 500 nm (except 30% which was 200 nm) and were grown on nitride substrates at 500 °C . The silicon substrates were thinned down to 70 μm . The measurements were of the in-plane magnetization (in zero applied field) after the film had been magnetized to saturation.

Figures 5.10, 5.11, 5.12, and 5.13, show the results of experimental values of in-

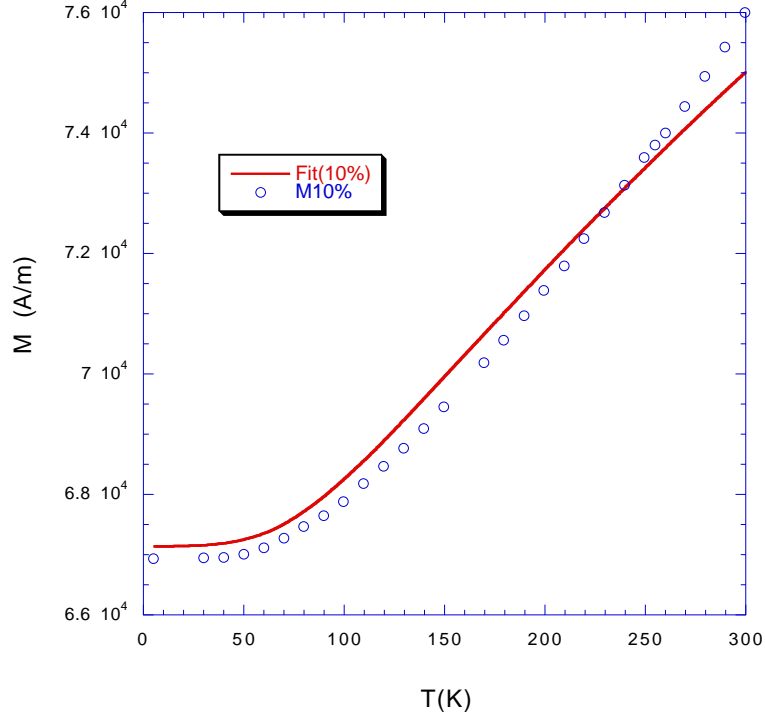


Figure 5.10: M_{ip} vs. T for Co: 10 wt%Ni film. Open circles are experimental data, solid line is fit by equation 5.1.

plane magnetization versus temperature. As predicted in the previous section, all data shows a pronounced knee at about 100 K and asymptotic behavior toward 0 K.

5.3.3.1 analysis

In fitting the data with equation 5.1 both the anisotropy (K_u) and the product of in-plane magnetostriction and applied stress had to be varied. However, the value of K_u was estimated from experimental data and the final parameter came close to the estimated value.

For the alloys lower in nickel, the fit is not as accurate. This is due to the fact that the model is less accurate because the value of magnetocrystalline anisotropy is close to the shape anisotropy ($\frac{\mu_0 M_s^2}{2}$). This is to be expected because as the nickel content is decreased, the alloy becomes more and more similar hcp cobalt. Magnetically this

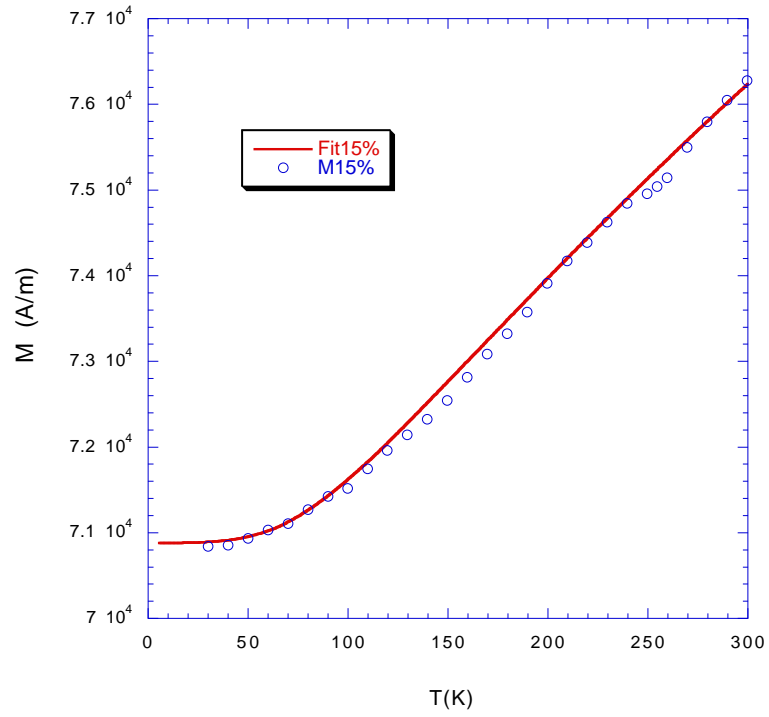


Figure 5.11: M_{ip} vs. T for Co: 15 wt%Ni film. Open circles are experimental data, solid line is fit by equation 5.1.

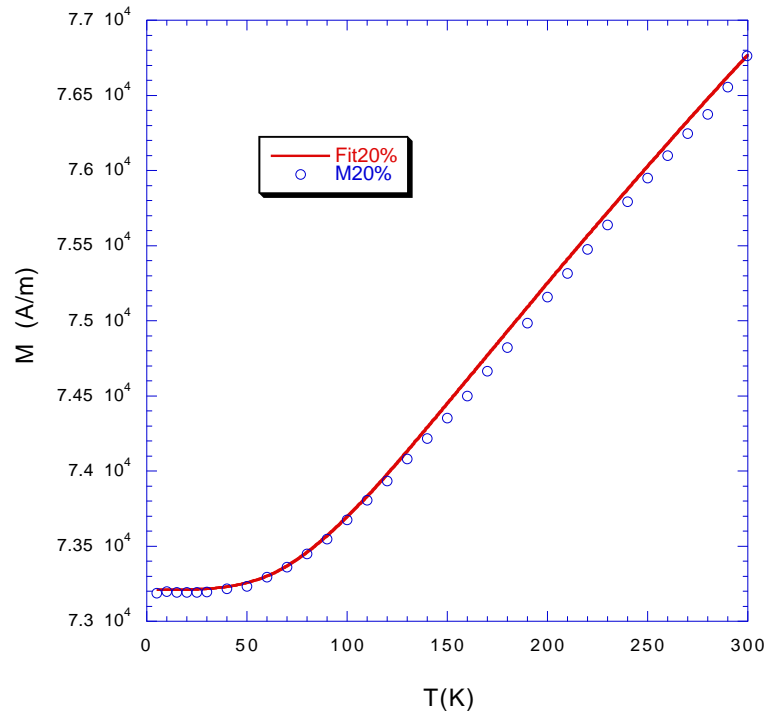


Figure 5.12: M_{ip} vs. T for Co: 20 wt%Ni film. Open circles are experimental data, solid line is fit by equation 5.1.

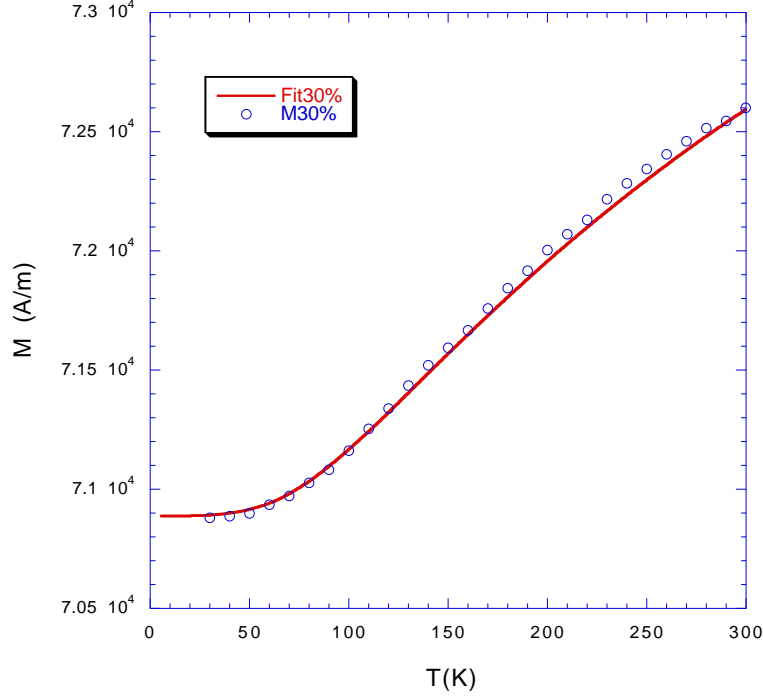


Figure 5.13: M_{ip} vs. T for Co: 30 wt%Ni film. Open circles are experimental data, solid line is fit by equation 5.1. Note the downward concavity as predicted in the previous section.

can be seen from the hysteresis data in chapter four. Although the curve matches the data for the lower nickel content films, the inaccuracy arises from the fact that the M_{ip} does not match up with M_s . Again, this can be explained by the magnetic data; in other words, at zero applied field the lower nickel content films have a remnant magnetic field less than M_s .

As the nickel content increases, the fit becomes extremely accurate. This is a testament to the simplicity of the model, because for the cubic films the estimate value of magnetocrystalline anisotropy is about, $0.13K_1^{cubic} + 0.17K_2^{cubic}$, which is about 10 times less than the shape anisotropy energy ($\frac{\mu_0 M_s^2}{2} \simeq 4 \times 10^3 \text{ J/m}^3$) for cubic (nickel rich films). Thus, the films with higher nickel content are very much close to being uniaxial with an easy plane and hard axis than the cobalt rich films with an easy magnetocrystalline axis perpendicular to the easy plane due to shape anisotropy. By comparison, the magnetocrystalline anisotropy of cobalt rich alloys is about twice

| wt%Ni | M_s (kA/m) | K_u (J/m ³) | $-\lambda_s^{ip}$ |
|-------|--------------|---------------------------|--------------------------|
| 10 | 100 | 8 ($\times 10^3$) | 7.2 ($\times 10^{-7}$) |
| 15 | 95 | 8.28 | 7.12 |
| 20 | 90 | 8.25 | 7.05 |
| 30 | 75 | 10.4 | 22.7 |

Table 5.1: *Magnetoelastic data for Co-Ni thin films.*

that of the more nickel rich alloys, but the shape anisotropy is only about 1/3 greater.

Table 5.1 summarizes the magnetoelastic values for the alloy films in this thesis derived from the best fit to magnetization versus temperature data. A few comments about this data are necessary: First, while the uniaxial anisotropy was a parameter, a small change in K_u changed the fit dramatically; so while K_u was flexible, once a value is chosen, the fit is fine-tuned only by changing λ_s . Secondly, since $\lambda_s^{ip}\sigma$ was a parameter, a value of elastic modulus must be chosen in order to determine σ and thus λ_s^{ip} . A value of 220 GPa was chosen, as this is close to the elastic modulus for both cobalt and nickel. Even though the elastic modulus can change for thin films (see e.g. [47]), the bulk value is within the accuracy of the measurement and the fit.

In support of the tabulated data, is the fact that the value of λ_s^{ip} determined by the fit is close to the value extrapolated from the cantilever measurement for a 500 nm Co: 20 wt%Ni film, this helps to validate the cantilever measurement technique developed. Also, it should be pointed out that the value of λ_s^{ip} for the 30 wt%Ni film is very similar to the bulk value of polycrystalline nickel.

This model is remarkably successful despite many unique elastic properties of thin films, and the fact that magnetocrystalline anisotropy can vary (even change sign) with temperature for cobalt and nickel. The fact that these issues did not affect the model significantly is because the films were polycrystalline (thus more bulk-like) and that the shape anisotropy dominated the magnetocrystalline anisotropy.

One last interesting feature is that λ_s^{ip} gets smaller with increasing Ni concentra-

tion until the film switches to a cubic phase, then λ_s^{ip} increases by a factor of four. This is because the value of magnetostriction is very small in the basal plane for hcp cobalt (when the applied field is in the basal plane).

5.4 conclusions and future work

Although the primary motivation of this thesis was the discovery and investigation of giant magnetostriction, as is often the case the experiments done in this thesis provided other interesting results, but not giant magnetostriction. Although the films grown and the measurements undertaken were fairly complete, there are some follow-up experiments worth considering.

5.4.1 future work

I feel the most interesting experiment to be done involves magnetic annealing. Figure 5.14 taken from [48] shows the results of annealing bulk Co-Ni alloys in modest (up to 8 kOe) magnetic fields. These results are interesting because of the relation between anisotropy and magnetostriction. From my results, the magnetocrystalline anisotropy has an interesting relationship with the magnetostriction. From table 5.1 one can see that for hexagonal films the increasing magnetocrystalline anisotropy goes with an increasing value of magnetostriction. It is interesting to investigate the effects of increasing the magnetocrystalline anisotropy (thus decreasing the uniaxial, or total, anisotropy).

In figure 5.14 the anisotropy follows a model developed by Neel that depends on the entropy of mixing. Thus the maximum is reached at 50 % concentration of Ni in Co. The value of magnetocrystalline anisotropy between about 65 % Co and 80 % Co is not explained by the Neel model. The anomalous behavior of the anisotropy in this composition would seem to indicate a strong coupling between structural

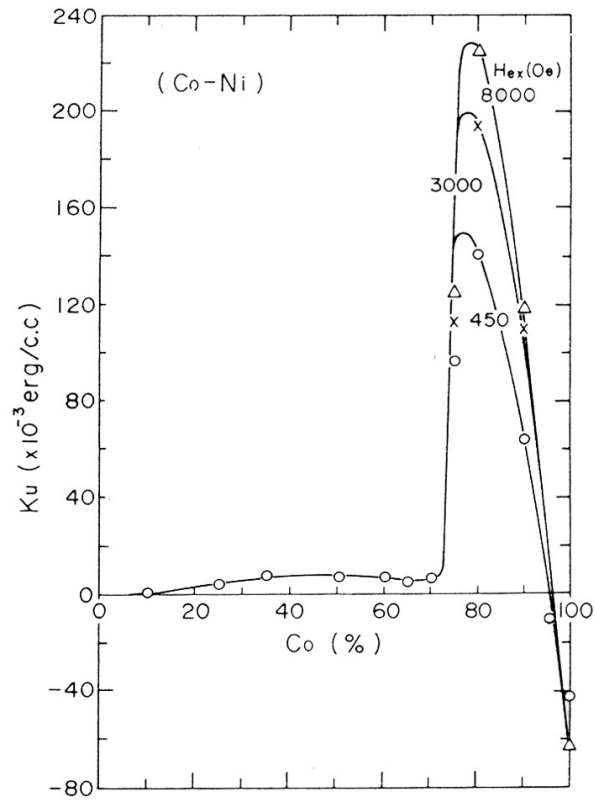


Figure 5.14: Data showing the variation of induced magnetocrystalline anisotropy with composition and applied field for Co-Ni alloys. Divide by 10 to get J/m³ from erg/cm³

and magnetic properties. Tanaka [49] shows that the grain structure of bulk Co-Ni alloys (less than 35 wt%Ni) is very sensitive to magnetic annealing conditions, and thus hypothesizes that the grain structure is the source of the anomalous induced anisotropy.

In light of these papers, it would be worthwhile to investigate how magnetic annealing affects the morphology, microstructure, and magnetoelastic properties of thin film Co-Ni alloys.

5.4.2 conclusion

The work in this thesis provides a number of interesting and important results.

- Constrained Co-Ni thin films have phase transformation different from the bulk. In particular, the constraint of the substrate tends to repress formation of the hexagonal phase.
- Bulk martensite microstructure and morphology was present in films as thin as 50 nm. This is an interesting result that suggests the thermodynamics of martensitic transformations in Co-Ni do not depend on the volume of the specimen, but depend only on other thermodynamic variables such as stress and temperature.
- Magnetization measurements provide an accurate and simple way to resolve the dominant phase of a Co-Ni thin film. X-ray diffraction is difficult to resolve a single specimen, and works best when one has a range of compositions to compare.
- A simple magnetoelastic measurement technique using optical recording and a special process to fabricate cantilever specimens can be used to measure magnetostriction to a high degree of accuracy.

- A simple uniaxial model based on the Stoner-Wolfarth model, provided an excellent fit to magnetization as a function of temperature. The parameters of the model can be used to calculate the uniaxial anisotropy and the in-plane value of magnetostriction.

Finally, values of magnetostriction were successfully measured (by the novel techniques described above) for the range of Co-Ni alloys from 10 wt%Ni to 35 wt%Ni, and it was found that no magnetic phase transformation was induced for the films in consideration.

Appendix A

Linear deformation using the strain tensor representation

In this appendix the strain in an arbitrary direction will be calculated by projecting a strain tensor onto a vector \vec{r}_0 . This proof is for a cubic system with strain tensor e_{ij} . The vector \vec{r}_0 makes cosines with the coordinate axes,

$$\beta_1 = \frac{x_0}{r_0}; \beta_2 = \frac{y_0}{r_0}; \beta_3 = \frac{z_0}{r_0}. \quad (\text{A.1})$$

Thus, to calculate the strain $r - r_0/r_0$, note that on application of a stress, projecting the strain tensor, e_{ij} , onto r_x gives

$$x = x_0(1 + e_{11}) + e_{12}y_0 + e_{13}z_0 \quad (\text{A.2})$$

with similar results for the y and z components of \vec{r} . Multiplying through by r_0/r_0 gives

$$x = r_0(\beta_1 + e_{1j}\beta_j) \quad (\text{A.3})$$

where the index j implies summation over $j = 1, 2, 3$. Now to find r , take

$$x^2 = r_0^2(\beta_1^2 + 2e_{1j}\beta_j\beta_1 + e_{1j}^2\beta_j^2) \quad (\text{A.4})$$

with similar results for y^2 and z^2 . Neglecting terms of order e_{ij}^2

$$\begin{aligned} r^2 &= r_0^2 \overbrace{(\beta_1^2 + \beta_2^2 + \beta_3^2)}^1 + e_{ij}\beta_i\beta_j \\ &= r_0^2(1 + e_{ij}\beta_i\beta_j) \Rightarrow \\ r &= r_0\sqrt{1 + e_{ij}\beta_i\beta_j} \end{aligned} \quad (\text{A.5})$$

where the summation is now taken over i, j . Using the binomial expansion

$$(1 + x)^a = 1 + \frac{x}{a} + \dots; \quad x < 1$$

where we assume the product $2e_{ij}\beta_i\beta_j < 1$ gives,

$$r = r_0(1 + e_{ij}\beta_i\beta_j) \Rightarrow \frac{r - r_0}{r_0} = e_{ij}\beta_i\beta_j. \quad (\text{A.6})$$

For e_{ij} real and Hermitian ($e_{ij}^* = e_{ji}^*$) we can rewrite the previous result as,

$$\begin{aligned} \beta_i e_{ij} \beta_j &= \begin{pmatrix} \beta_1 e_{11} \beta_1 & \beta_1 e_{12} \beta_2 & \beta_1 e_{13} \beta_3 \\ \beta_2 e_{21} \beta_1 & \beta_2 e_{22} \beta_2 & \beta_2 e_{23} \beta_3 \\ \beta_3 e_{31} \beta_1 & \beta_3 e_{32} \beta_2 & \beta_3 e_{33} \beta_3 \end{pmatrix} \\ &= \frac{\partial l}{l} = \sum_i e_{ii} \beta_i^2 + \sum_{i < j} e_{ij} \beta_i \beta_j. \end{aligned} \quad (\text{A.7})$$

Thus equation A.7 gives you the elastic strain in a cubic system for an arbitrary direction, described by $[\beta_1, \beta_2, \beta_3]$, due to a strain e_{ij} .

Appendix B

Stress dependence of \vec{M}_{ip}

The following is a derivation of the in-plane component of magnetization, as a function of stress, of a thin film. The stress is the result of an imposed strain due to mismatch in the coefficient of thermal expansion (CTE) of the film and the substrate. For the following derivation, M_s is the saturation value of magnetization, σ is the applied stress, λ_s is the in-plane value of magnetostriction, and the angle between the magnetic moment and the film normal is $\frac{\pi}{2} - \theta$. Figure B.1 shows the geometry of the problem. The procedure is to write down an expression for the total magnetic

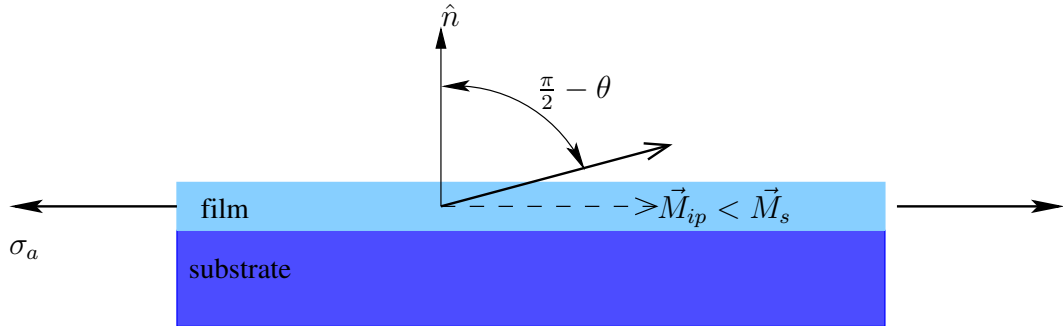


Figure B.1: *At saturation the net magnetic moment is M_s . When λ_s is less than zero, a positive tensile stress causes the magnetic moment to deviate from in-plane, thus the measured in-plane moment, M_{ip} is less than M_s .*

energy, and then minimize as a function of θ and solve for the in-plane magnetization (which is the experimentally measured quantity). For simplicity, $M_{ip} = M_s \cos \theta$ is

written as M .

The Stoner-Wolfarth model gives the following values for magnetic energy [25]

The magnetostatic energy is

$$u_{ms} = \frac{\mu_0 M_s^2}{2} \sin^2 \theta. \quad (\text{B.1})$$

The magnetoelastic energy is

$$u_{me} = -\frac{3}{2} \lambda_s \sigma_a \sin^2 \theta. \quad (\text{B.2})$$

The total magnetic anisotropy energy¹ is

$$u_a = -K_u \cos^2 \theta. \quad (\text{B.3})$$

So the total energy is

$$u_{total} = \frac{\mu_0 M_s^2}{2} \sin^2 \theta - K_u \cos^2 \theta - \frac{3}{2} \lambda_s \sigma_a \sin^2 \theta \quad (\text{B.4})$$

and

$$\frac{\partial u_{total}}{\partial \theta} = \frac{\mu_0 M_s^2}{2} \cos \theta - 2K_u \cos \theta \sin \theta - 3\lambda_s \sigma_a \sin \theta \cos \theta = 0 \quad (\text{B.5})$$

in equilibrium. With $M \equiv M_s \cos \theta$, $\cos \theta = M/M_s$ and substituting

$$\sin \theta = \sqrt{1 - \cos^2 \theta} = \sqrt{1 - \left(\frac{M}{M_s}\right)^2}$$

gives the result

$$M = M_s \sqrt{1 - \left(\frac{\mu_0 M_s^2}{4K_u + 6\lambda_s \sigma_a}\right)^2}. \quad (\text{B.6})$$

In ideal uniaxial systems a further simplification can be made by substituting

¹ K_u is the uniaxial anisotropy coefficient (to first order) which is $\frac{\mu_0 M_s H_a}{2}$, where H_a is the field needed to saturate the sample in the hard direction.

$K_u = \frac{\mu_0 M_s H_a}{2}$ to get

$$M = M_S \sqrt{1 - \left(\frac{\mu_0 M_s^2}{6\lambda_s \sigma_a + 2\mu_0 M_s H_a} \right)^2}. \quad (\text{B.7})$$

Equation B.7 is particularly useful, because one only needs to measure M_s and H_a to apply this model and determine λ_s for a particular film.

Bibliography

- [1] E. L. Houston and D. T. Peters. Magnetic and magnetostrictive properties of cube textured nickel for magnetostrictive transducer applications. *IEEE Transactions on Magnetics*, MAG-9:636–640, 1973.
- [2] G. Y. Chin. Processing control of magnetic properties for magnetostrictive transducer applications. *Journal of Metals*, 1:42–45, 1971.
- [3] M. R. J. Gibbs and R. Watts. Microstructures containing piezomagnetic elements. *Sensors and Actuators A*, 59:229–235, 1997.
- [4] A. Ludwig and E. Quandt. Giant magnetostrictive thin films for application in microelectromechanical systems. *Journal of Applied Physics*, 87 No. 9:4691–4695, 2000.
- [5] M Wuttig and L. Liu. Occurrence of ferromagnetic shape memory alloys. *Journal of Applied Physics*, 87 No. 9:4707–4711, 1998.
- [6] B. D. Cullity. Fundamentals of manetostriction. *Journal of Metals*, 1:35–41, 1971.
- [7] F. Schatz and M. Hirscher. Magnetic anisotropy and giant magnetostriction of amorphous TbDyFe films. *Journal of Applied Physics*, 76 No. 9:5380–5382, 1994.
- [8] H. Szymczak. From almost zero magnetostriction to giant magnetostrictive effects: recent results. *Journal of Magnetism and Magnetic Materials*, 200:425–438, 1999.

- [9] C. Zenner. Impact of magnetism upon metallurgy. *Journal of Metals*, 1:619–630, 1955.
- [10] R. D. James and K. F. Hane. Martensitic transformations and shape-memory materials. *Acta materialia*, 48:197–222, 2000.
- [11] K. Otsuka and C. M. Waymans, editors. *Shape Memory Materials*. Cambridge, 2000.
- [12] X. Ren and K. Otsuka. Origin of rubber-like behavior in metal alloys. *Nature*, 389 No. 9:579–581, 1997.
- [13] H. Sakamoto and K. Otsuka. Rubber-like behavior in a Cu – Al – Ni alloy. *Scripta Metallurgica*, 11:607–611, 1977.
- [14] J. W. Christian. *The Theory of Phase Transformations in Metals and Alloys*, chapter 16. Pergamon Press, 1981.
- [15] R. C. O’Handley and S. J. Murray. Phenomenology of giant magnetic-field induced strain in ferromagnetic shape-memory materials. *Journal of Applied Physics*, 87 No. 9:4712–4717, 2000.
- [16] R. C. O’Handley. Model for strain and magnetization in magnetic shape-memory alloys. *Journal of Applied Physics*, 83 No. 6:3263–3270, 1998.
- [17] G. H. Wu and W. H. Wang. Magnetic properties and shape memory of Fe doped $\text{Ni}_{52}\text{Mn}_{24}\text{Ga}_{24}$ single crystals. *Applied Physics Letters*, 80 No. 4:634–636, 2002.
- [18] A. Sozinov and A.A. Likhachev. Giant magnetic-field-induced strain in NiMnGa seven-layered martensitic phase. *Applied Physics Letters*, 80 No. 10:1746–1748, 2002.

- [19] T. Kakeshita and T. Takeuchi. Giant magnetostriction in an ordered Fe₃Pt single crystal exhibiting a martensitic transformation. *Applied Physics Letters*, 77 No. 10:1502–1504, 2000.
- [20] T. Kakeshita and K. Ulakko. Giant magnetostriction in ferromagnetic shape-memory alloys. *MRS Bulletin*, 27 No. 2:105–109, 2002.
- [21] R. C. O’Handley. *Modern Magnetic Materials Principles and Applications*, chapter 7. John Wiley and Sons, Inc., 2000.
- [22] Y. Liu and W. M. Zhou. Magneto-shape-memory effect in CoNi single crystals. *Applied Physics Letters*, 78 No. 23:3660–3662, 2000.
- [23] K. Oikawa, L. Wulff, F. Gejima, and T. Ohmori. Promising ferromagnetic Ni – Co – Al shape memory alloys. *Applied Physics Letters*, 79 No. 20:3290–3292, 2001.
- [24] C. W. Chen. *Magnetism and Metallurgy of Soft Magnetic Materials*, chapter 3. Dover Publications, 1986.
- [25] S. Chikazumi. *Physics of Ferromagnetism*, chapter 14. Oxford University Press., 1997.
- [26] K. R. Symon, editor. *Mechanics*, chapter 10. Addison-Wesley, 1971.
- [27] J. S. Bowles and J. K. Mackenzie. The crystallography of martensite transformations. *Acta Metallurgica*, 2:129–147, 1954.
- [28] A. G. Khachaturyan. *Theory of Structural Transformations in Solids*, chapter 1. John Wiley and Sons, Inc., 1983.
- [29] Zenji Nishiyama. *Martensitic Transformation*. Academic Press, 1978.

- [30] A. G. Khachaturyan. *Theory of Structural Transformations in Solids*, chapter 6. John Wiley and Sons, Inc., 1983.
- [31] B. E. Warren, editor. *X-ray Diffraction*, chapter 13. Dover, 1990.
- [32] E. Votava. The phase transformation in thin cobalt films. *Journal of The Institute of Metals*, 90:129–132, 1961.
- [33] J. B. Hess and C. S. Barrett. Transformation in cobalt-nickel alloys. *Journal of Metals*, 1:645–647, 1952.
- [34] H. Maeda. High coercivity cobalt and cobalt-nickel alloy films. *Journal of Applied Physics*, 53 No. 5:3735–3739, 1982.
- [35] J-H. Jun, T-J Ha, and C-S Choi. The effect of deformation on microstructure and damping capacity in a Co – Ni alloy. *Scripta Materialia*, 43 No. 7:603–608, 2000.
- [36] E. Votava. Electron microscopic investigation of the phase transformation of thin cobalt samples. *Acta Metallurgica*, 8:901–904, 1960.
- [37] P. Gaunt and J. W. Christian. The cubic-hexagonal transformation in single crystals of cobalt and cobalt-nickel alloys. *Acta Metallurgica*, 7:529–533, 1959.
- [38] W. L. Winterbottom. Equilibrium shape of a small particle in contact with a foreign substrate. *Acta Metallurgica*, 15:303–310, 1967.
- [39] P. G. Schultz and X. Xiang. Combinatorial approaches to materials science. *Journal of Solid State Chemistry*, 3:1–11, 1998.
- [40] Donald L. Smith. *Thin Film Deposition*, chapter 5. McGraw-Hill Inc., 1995.
- [41] A. Taylor. Lattice parameters of binary nickel-cobalt alloys. *Proceedings of The Royal Society*, 77:585–594, 1950.

- [42] E. T. de Lacheisserie. *Magnetostriction*. CRC Press, 2001.
- [43] R. C. Wetherhold and H. D. Chopra. Beam model for calculating magnetostriction strains in thin films and multilayers. *Applied Physics Letters*, 79 No. 23:3818–3820, 2001.
- [44] E. T. de Lacheisserie and J. C. Peuzin. Magnetostriction and internal stresses in thin films: the cantilever method revisited. *Journal of Magnetism and Magnetic Materials*, 136:189–196, 1994.
- [45] Stanford University Professor W. Nix. Stress in thin films, class notes.
- [46] Y.S. Touloukian and R.K. Kirby. *Thermal Expansion* metallic elements and alloys, volume 12. Plenum, 1979.
- [47] J. Gump, H. Xia, M. A. Tomaz, and G. R. Harp. Elastic constants of face-centered-cubic cobalt. *Journal of Applied Physics*, 86 No. 11:6005–6009, 2000.
- [48] M. Takahashi and Tatsuo Kono. Magnetic anisotropy induced by magnetic and stress annealing in Co, Co – Ni, and Co – Fe alloys. *Japanese Journal of Applied Physics*, 17 No. 2:361–369, 1978.
- [49] T. Tanaka, M. Takahashi, and S. Kadowaki. Induced uniaxial magnetic anisotropy and preferred orientation in cobalt and cobalt-nickel alloy by magnetic annealing. *Journal of Applied Physics*, 84 No. 12:6768–6772, 1998.